Cell Stem Cell

Short article

Generation of human region-specific brain organoids with medullary spinal trigeminal nuclei

Graphical abstract

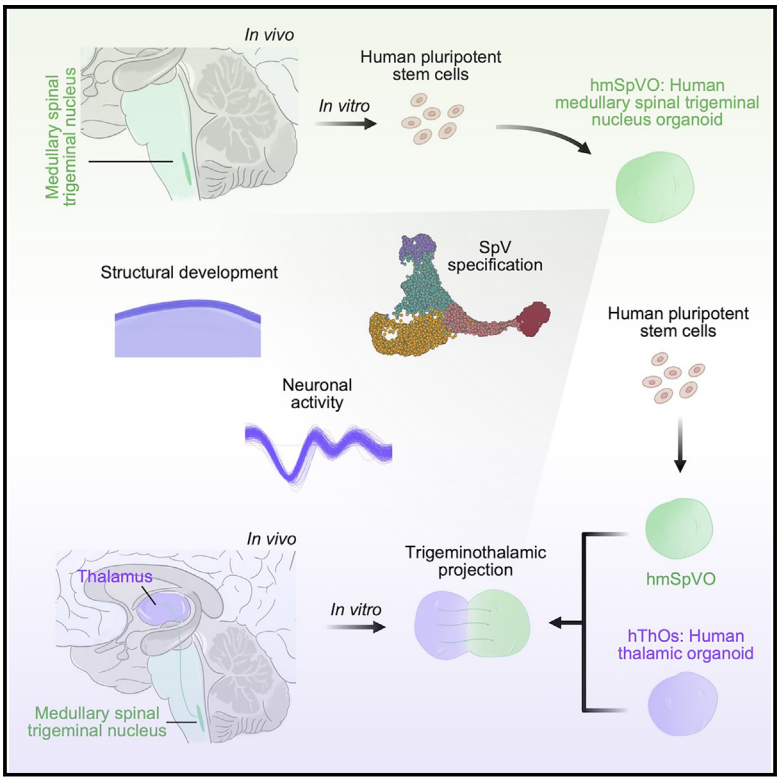

Highlights

- Human medullary SpV-like organoids (hmSpVOs) are created from hPSCs
- hmSpVOs resemble the spinal trigeminal nucleus (SpV) of the dorsal medulla
- hmSpVOs exhibit structural and functional maturation in long-term culture
- Trigeminothalamic tracts are established between hmSpVOs and thalamic organoids

Authors

Wei Pang, Jinkui Zhu, Kexin Yang, ..., Yao Yin, Ziling Chen, Yangfei Xiang

Correspondence

xiangyf@shanghaitech.edu.cn

In brief

Generating brain organoids with nucleus-specific identities is challenging. Xiang and colleagues report a method for generating human region-specific brain organoids that recapitulate the medullary spinal trigeminal nucleus (SpV) and the trigeminothalamic connection. These findings provide an accessible model for studying the human SpV, its associated circuits, and brain diseases.

Pang et al., 2024, Cell Stem Cell *31*, 1501–1512
October 3, 2024
https://doi.org/10.1016/j.stem.2024.08.004

CellPress

Cell Stem Cell

CellPress
OPEN ACCESS

Short article

Generation of human region-specific brain organoids with medullary spinal trigeminal nuclei

Wei Pang,[1,4] Jinkui Zhu,[1,4] Kexin Yang,[1] Xiaona Zhu,[1] Wei Zhou,[1] Linlin Jiang,[1] Xuran Zhuang,[1] Yantong Liu,[1] Jianfeng Wei,[1] Xiaoxiang Lu,[1] Yao Yin,[1] Ziling Chen,[1] and Yangfei Xiang[1,2,3,5,*]

[1]School of Life Science and Technology, ShanghaiTech University, Shanghai 201210, China
[2]State Key Laboratory of Advanced Medical Materials and Devices, ShanghaiTech University, Shanghai 201210, China
[3]Shanghai Clinical Research and Trial Center, Shanghai 201210, China
[4]These authors contributed equally
[5]Lead contact
*Correspondence: xiangyf@shanghaitech.edu.cn
https://doi.org/10.1016/j.stem.2024.08.004

SUMMARY

Brain organoids with nucleus-specific identities provide unique platforms for studying human brain development and diseases at a finer resolution. Despite its essential role in vital body functions, the medulla of the hindbrain has seen a lack of *in vitro* models, let alone models resembling specific medullary nuclei, including the crucial spinal trigeminal nucleus (SpV) that relays peripheral sensory signals to the thalamus. Here, we report a method to differentiate human pluripotent stem cells into region-specific brain organoids resembling the dorsal domain of the medullary hindbrain. Importantly, organoids specifically recapitulated the development of the SpV derived from the dorsal medulla. We also developed an organoid system to create the trigeminothalamic projections between the SpV and the thalamus by fusing these organoids, namely human medullary SpV-like organoids (hmSpVOs), with organoids representing the thalamus (hThOs). Our study provides a platform for understanding SpV development, nucleus-based circuit organization, and related disorders in the human brain.

INTRODUCTION

Over the past decade, from unguided cerebral organoids[1] to various region-specific brain organoids constructed through guided differentiation,[2–5] and more complex organoids that integrate interplay between multiple lineages or brain regions (namely, assembloids),[6–12] brain organoids represent a cutting-edge strategy for unraveling the biology of the human brain. Although various region-specific brain organoids have been established, the endeavor to recapitulate brain-nucleus-specific features is still in its early stages. We recently developed an approach to model the human thalamic reticular nucleus in ventralized human thalamic organoids.[13] An earlier report established a method to generate human hypothalamic organoids with an arcuate-nucleus-like feature.[14] The generation of brain-nucleus-specific cells in a two-dimensional (2D) culture is also possible.[15] Nevertheless, considering the variety of functional nuclei in the brain, the availability of region-specific brain organoids with nucleus-specific features is still limited, and nucleus-specific brain circuits have not yet been modeled with human cells. Region-specific brain organoids recapitulating nucleus-specific signatures will facilitate a more precise and in-depth understanding of the human brain.[16]

The spinal trigeminal nucleus (SpV), the largest cranial nerve nucleus spanning the entire brainstem, is one of the essential components of the trigeminal nucleus. The SpV can be further divided into three subnuclei: oral subnucleus (Vo), interpolar subnucleus (Vi), and caudal subnucleus (Vc). Whereas Vo and Vi are associated with tactile sense, Vc, located in the medulla, is the nucleus responsible for relaying nociception and thermal sensations from the head to the thalamus, which is crucial for maintaining normal physiological functions of the body. Although the SpV plays critical roles in sensory processing and modulation, neuralgia etiology, and even pathogen-caused pathological reactions, there is currently no model for the human SpV. Here, we applied guided three-dimensional (3D) differentiation of human pluripotent stem cells (hPSCs) and developed a method for generating human region-specific brain organoids with specific signatures of the medullary SpV, namely human medullary SpV-like organoids (hmSpVOs). We dissected lineage specification during hmSpVO development by single-cell transcriptome and profiled the structural and functional maturation of hmSpVOs. We subsequently constructed an organoid model to recapitulate the trigeminothalamic projections between the human SpV and thalamus by fusing hmSpVOs with thalamic organoids (hThOs)[12] to form human fused SpV-thalamus organoids (hSTOs). We anticipate that our approach will provide an accessible *in vitro* model for future studies of the human SpV, its associated neural circuits, and related brain diseases.

RESULTS

Generation of hmSpVOs from hPSCs

To identify differentiation conditions for medullary SpV development, a static-to-spinning 3D culture strategy we previously established was applied.[8,11–13] Uniform embryoid bodies (EBs) were produced from dissociated H9 human embryonic stem cells (hESCs). Dual SMAD inhibition was applied to induce the neuroectoderm fate, along with the supplement of CHIR99021 (a WNT activator) and retinoic acid (RA). WNT and RA are caudalization cues essential for hindbrain development, while WNT signaling also induces dorsal patterning.[17–19] Among the conditions screened (representative conditions listed in Figure S1A), we identified combinations of WNT and RA treatments that could achieve a confined differentiation of the dorsal-caudal hindbrain, potentially with a rhombomeres r7/8 signature of the medulla (e.g., C6 and C9, Figures S1B–S1F). The dorsal part of the medullary hindbrain contains two major progenitor domains: OLIG3$^+$ class A progenitors, located the most dorsally, and the more ventrally located class-B progenitors that generate ladybird homeobox 1 (LBX1)$^+$ neurons from which SpV neurons derive (Figure S1G).[19] Specifically, medullary dBLa and dBLb domains, both of which develop from the dB1 domain, generate the inhibitory neurons (InNs) and excitatory neurons (ExNs) of the SpV, respectively.[19–21] Transcriptomic analysis identified that organoids derived from candidate condition (i.e., C9, hereafter referred to as the hmSpVO strategy; Figure 1A) showed the highest similarity with dBLb, dBLa, and the closely related dB1 domains (Figure S1H). qPCR analysis also revealed that hmSpVOs possessed a class-B-like feature, which could be efficiently shifted dorsally or ventrally through BMP4 or SHH treatment (Figures S1I and S1J). Because long-time WNT activation enhanced neuroepithelium expansion, we added dissolved Matrigel (1% v/v) to hmSpVO culture to assist the folding of neuroepithelium tissue (Figure 1A). RNA sequencing (RNA-seq) analysis of hmSpVOs replicates further validated their hindbrain-specific identity, distinct from hESCs and our previously established human cortical organoids (hCOs)[8] (Figure 1B). The expression of Homeobox (HOX) gene paralog groups 3–4 also revealed a correlation of hmSpVOs with the caudal hindbrain where the medulla develops (Figure 1B),[19,22] consistent with transcriptomic similarity analysis (Figure S1E). We also confirmed that 4 different hPSC lines (H9 and H1 hESC lines and hiPSC lines RC01001A and RC01001B) could establish similar rostral-caudal identities during hmSpVOs differentiation, in contrast to hCOs, hThOs, and H9 hESCs (Figure 1C).

RNA-seq analysis also revealed that while hmSpVOs replicates showed high similarity with dBLb, dBLa, and their related dB1 domains, this region-specific identity could be diminished when ventral patterning was applied (Figure 1D), again indicating the relevance of SpV development in hmSpVOs. We then validated the generation of SpV-related lineages in hmSpVOs through immunostaining. Early stage (day 16) hmSpVOs were enriched with PAX7$^+$ and SOX2$^+$ progenitors and started to produce PAX2$^+$ and LMX1B$^+$ differentiated cells; in contrast, neither hThOs nor hCOs showed abundant production of these cell types except for the presence of SOX2$^+$ progenitors (Figures 1E and S2A–S2C). Similarly, cells positive for PAX2 and LIM homeobox 1/5 (LHX1/5), essential for SpV InN differentiation, were uniquely generated in hmSpVOs but not in hThOs and hCOs (Figure 1F). Also consistent with transcriptomic analysis, hmSpVOs did not show evident production of OLIG3$^+$ class A lineage or ventrally located lineages labeled by NKX6-1, PHOX2B, or NKX2-2 (Figures S2D–S2F). Besides, no SOX10-positive neural crest lineage was detected in hmSpVOs, like hThOs and hCOs (Figures S2A–S2C). Abundant LMX1B$^+$ cells and PAX2$^+$/LHX1/5$^+$ cells could be produced in hmSpVOs after longer culture (day 30, Figures 1G–1I), indicating the development of SpV-relevant excitatory and inhibitory neuronal lineages, respectively.[19,21] The identities of LMX1B$^+$ and PAX2$^+$ cells were validated through immunostaining with the excitatory marker vesicular glutamate transporter type 2 (vGLUT2) and the inhibitory marker gamma-aminobutyric acid (GABA) (Figures 1J and 1K). Notably, the homeodomain factor LBX1, which marks class-B neurons in the medulla and determines a somatosensory fate of relay neurons in the SpV,[20] was also found widely expressed in hmSpVOs but not in hThOs or hCOs (Figure 1L). As we previously reported,[8,12] hCOs and hThOs were able to generate TBR1$^+$ cortical neurons and TCF7L2$^+$ thalamic neurons, respectively, both of which were barely produced in hmSpVOs (Figures 1M and 1N), again indicating the distinct regional identity of hmSpVOs. Besides hmSpVOs from H9 hESCs, hmSpVOs derived from H1 hESCs, and hiPSC lines RC01001A and RC01001B, all showed similar lineage development (Figures S2G–S2N), and quantification revealed enriched production of PAX2$^+$ and LMX1B$^+$ cells specifically in hmSpVOs derived from all cell lines compared with hThOs and hCOs (Figure 1I), indicating the reliability of hmSpVO generation across different hPSC lines.

Single-cell transcriptomics reveals SpV lineage specification in hmSpVOs

To further analyze the regional identity and lineage specifications of hmSpVOs, we profiled the single-cell transcriptome of 7,214 cells derived from hmSpVOs at two developmental time points (days 30 and 62) (Figure 2A). Uniform manifold approximation and projection (UMAP) dimensionality identified 14 clusters, which were further categorized into 5 major cell types, including neural progenitor cell (NPC), intermediate progenitor (IP), immature neuron (IM), ExN, and InN (Figures 2A, 2B, S3A, and S3B). To understand the regional identity of hmSpVOs, we integrated organoid profiles with the human fetal brain atlas,[23] which showed that hmSpVOs most closely resemble the medulla of the human brain (Figures 2C, 2D, S3C, and S3D). Comparison with different cell types from human tissues validated the relevance of annotated cell clusters (Figure 2D, right). Expression of various HOX gene paralog groups 3–4 in hmSpVO-derived cells again confirmed their medullary identity (Figure S3E). We also applied VoxHunt,[24] which spatially maps single-cell RNA-seq (scRNA-seq) data onto mouse *in situ* hybridization data from the Allen Brain Atlas; the analysis revealed that hmSpVOs showed the highest correlation with the medulla of the mouse hindbrain (Figures S3F and S3G).

We found that for the hmSpVO-derived ExN group, the transporter vGLUT2, but not vGLUT1, was mainly expressed (Figure 2B), corroborating the *in vivo* observation that the medullary SpV mainly expresses vGLUT2.[25] The expressions of canonical markers for dBLa and dBLb, where the SpV develops, were

CellPress
OPEN ACCESS

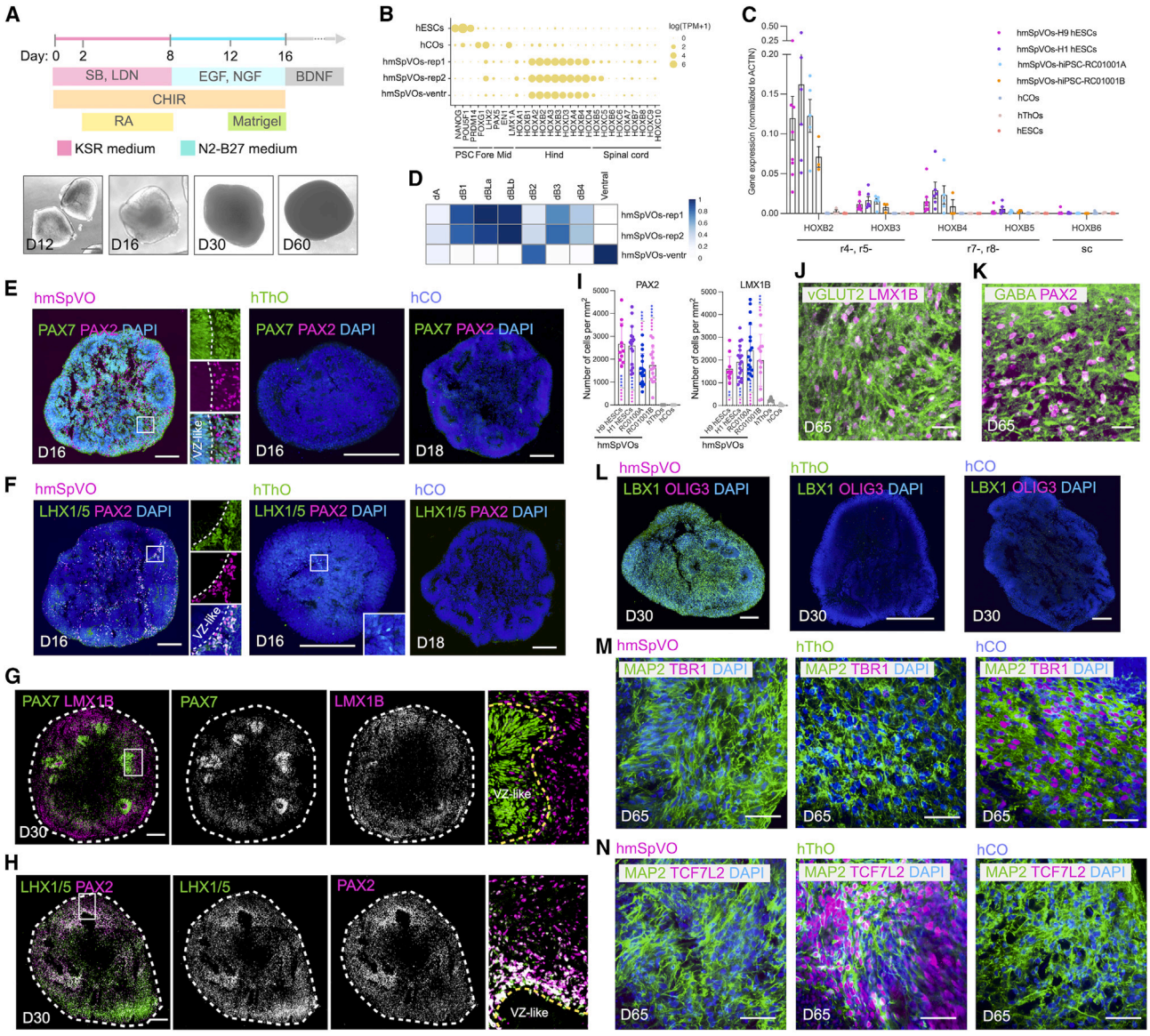

Figure 1. Generation of hmSpVOs from hPSCs

(A) Schematic showing the differentiation condition for hmSpVOs (top) and morphology of hmSpVOs at different developmental stages (bottom). SB, SB431542; LDN, LDN193189; CHIR, CHIR99021; RA, retinoic acid; EGF, epidermal growth factor; NGF, nerve growth factor; BDNF, brain-derived neurotrophic factor.

(B) Expression of region-specific genes in hmSpVOs compared with other samples based on bulk RNA-seq. Dot size represents log (TPM + 1) of each gene.

(C) qPCR analysis of HOX gene expressions in day 30 hmSpVOs derived from different hPSC lines. Data represent mean ± SEM (n = 9 repeats for H9 hESC-derived hmSpVOs, n = 5 repeats for H1 hESC-derived hmSpVOs, n = 4 repeats for hiPSCs RC01001A-derived hmSpVOs, n = 2 repeats for hiPSCs RC01001B-derived hmSpVOs, n = 4 repeats for hCOs, n = 3 repeats for hThOs, and n = 3 repeats for H9 hESCs).

(D) Similarity analysis of day 30 hmSpVOs and ventralized hmSpVOs with different neural subgroups of the medulla.

(E and F) Immunostaining of hmSpVOs, hThOs, and hCOs for PAX7 and PAX2 (E), LHX1/5 and PAX2 (F).

(G and H) Immunostaining of hmSpVOs for PAX7 and LMX1B (G), LHX1/5 and PAX2 (H).

(I) Quantification of PAX2$^+$ and LMX1B$^+$ cells in day 30 hmSpVOs derived from different hPSC lines. Data represent the mean ± SD (n = 8, 9, 9, and 8 organoids from 3 batches for H9 hESC-, H1 hESC-, RC01001A hiPSC-, and RC01001B hiPSC-derived hmSpVOs, respectively; n = 4 from 2 batches for hCOs and hThOs; 1–2 random slices were quantified for each organoid; $^*p < 0.05$, $^{**}p < 0.01$, $^{***}p < 0.001$, $^{****}p < 0.0001$, with red symbols indicating comparison to hThOs and blue indicating comparison to hCOs). Multiple comparison analysis test with ANOVA was used for statistical analysis.

(J and K) Immunostaining of hmSpVOs for vGLUT2 and LMX1B (J), GABA, and PAX2 (K).

(L) Immunostaining of hmSpVOs, hThOs, and hCOs for LBX1 and OLIG3.

(M and N) Immunostaining for MAP2 and TBR1 (M), MAP2 and TCF7L2 (N) in hmSpVOs, hThOs, and hCOs.

Scale bars: 500 μm in (A); 200 μm in (E)–(H) and (L); and 50 μm in (J), (K), (M), and (N).

See also Figures S1 and S2.

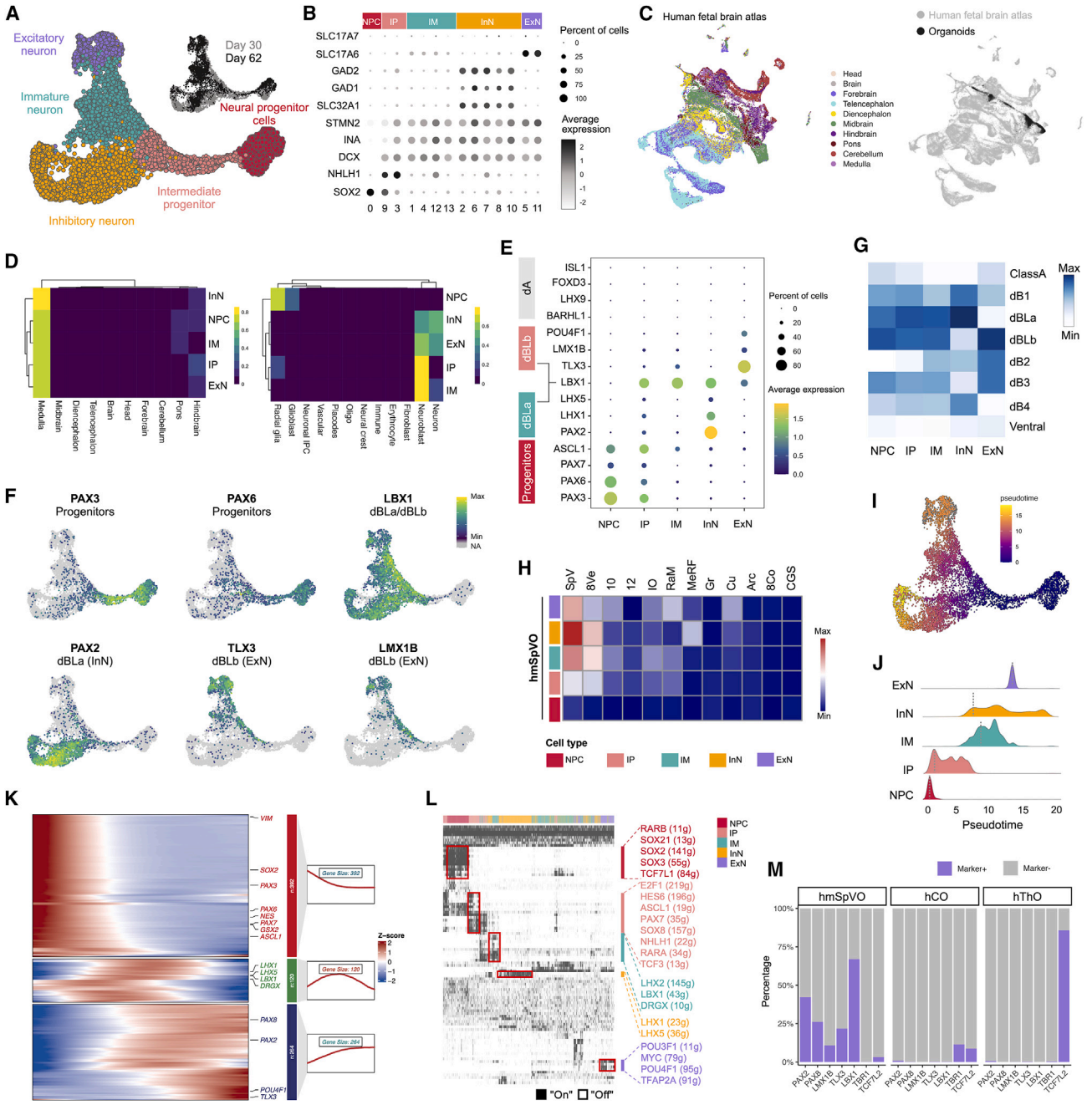

Figure 2. Single-cell transcriptomic analysis of hmSpVOs

(A) UMAP embedding of scRNA-seq data of 7,214 cells from hmSpVOs at day 30 (4,176 cells) and day 62 (3,038 cells).

(B) Dot plots showing the expression of cell-type-specific genes in each cluster of hmSpVOs.

(C) UMAP plots of the human fetal brain atlas (left) and integrated profiles (right).

(D) Heatmap of the region (left) and cell type (right) similarity between hmSpVOs and the human fetal brain (5–14 postconceptional weeks [pcw]).

(E) Dot plots showing the expression of dorsal medulla subregion-specific genes in each cluster of hmSpVOs.

(F) Feature plots showing the expression of cell-type-specific genes in hmSpVOs.

(G) Heatmap showing the similarity between different dorsal-ventral subregions of the medulla (genes were obtained from a mouse medulla oblongata development review; see STAR Methods) and different cell types of hmSpVOs.

(H) Heatmap showing the similarity between different human medullary nuclei (24–57 years old) and different cell types in hmSpVOs.

(I) Trajectory analysis showing the pseudotime of cells in hmSpVOs.

(J) Ridgeline plot showing the pseudotime of cell types in hmSpVOs.

(legend continued on next page)

examined, and, as found *in vivo*, dBLa-specific genes like PAX2, LHX1, and LHX5 were mainly expressed in the InN group, whereas dBLb-specific genes, including TLX3, LMX1B, and POU4F1, were mainly detected in the ExN group; LBX1, the marker for class-B neurons that also defines somatosensory fate, was widely expressed in various cell clusters, except for NPC (Figures 2E, 2F, and S3H). In contrast, PHOX2B, a key factor for viscerosensory specification in other hindbrain nuclei, was not expressed (Figure S3H). Analysis of gene signatures for different developing domains of the hindbrain again revealed that InNs and ExNs in hmSpVOs most closely resemble the dBLa and the dBLb domain, respectively (Figure 2G). These data were in line with bulk RNA-seq and immunostaining analysis (Figures 1D–1K) and were consistent with the fact that the dBLa and dBLb domains are respectively responsible for generating SpV InNs and ExNs *in vivo*,[19–21] thus validating the specification of distinct SpV lineages in hmSpVOs.

To further verify subregion-specific identity, we compared the transcriptomic signatures of hmSpVOs with those of different human medullary nuclei using the Allen Brain Adult Human database (see STAR Methods). Notably, hmSpVO-derived cells most closely resembled the human SpV (Figure 2H). Besides, it is known that the SpV is an elongated structure spanning the pons and medulla of the hindbrain and can be divided into the Vo, Vi, and Vc, among which the Vc is in the medulla (Figure S3I). Our results, which showed that hmSpVOs exhibited the highest similarity with the medulla, suggest that SpV-related cells in hmSpVOs might possess a Vc-like identity. We thus surveyed the expressions of known markers for Vo, Vi, and Vc in both ExN and InN groups.[26] Indeed, the ExN group more closely resembled the Vc region than Vo and Vi; nevertheless, the InN group did not show a specific preference toward Vo, Vi, or Vc regions (Figure S3J). Future studies on human brain tissues at single-cell resolutions will be beneficial to understanding whether human SpV excitatory projection neurons possess a more confined brain-subregion-specific signature than SpV InNs.

We next performed pseudotime analysis in samples of two stages (days 30 and 62) to understand the developmental trajectory of different cell types in hmSpVOs. We found a clear early-to-late-stage transition from the NPC group to the InN and ExN groups (Figures 2I and S3K). RNA velocity analysis revealed a similar developmental relationship between different cell types (Figure S3K). Interestingly, while NPCs and IPs showed the earliest onset of genesis, as expected, InNs exhibited an earlier onset than ExNs in hmSpVOs (Figure 2J). Analysis of gene expression at different inferred states also revealed three major clusters, among which the expression of progenitor-related genes like VIM, SOX2, and PAX7 showed the earliest onset and decreased over time; following the first cluster was a cluster of genes defining the somatosensory fate, like LBX1, and genes essential to inhibitory neurogenesis, like LHX1 and LHX5; critical regulators for excitatory neurogenesis, like TLX3 and POU4F1, started to express in the latest cluster (Figure 2K). The correlation between essential transcription factors and the corresponding cell types was further verified through single-cell regulatory network inference and clustering (SCENIC), suggesting their roles in cell fate decisions during SpV development (Figures 2L and S3L). Further, a comparison with scRNA-seq data from other region-specific brain organoids we established, including hCOs and hThOs,[8,12] also revealed an SpV-specific identity of hmSpVOs (Figures S3M and S3N). Quantification of the specific cell populations involved in development of the SpV, cortex, or thalamus further verified the distinct regional identity of hmSpVOs compared with hCOs and hThOs (Figure 2M). Together, our results demonstrate that hmSpVOs recapitulate lineage specifications in the medullary SpV and facilitate dissecting neurogenesis and essential regulators in human SpV development.

Long-term structural and functional maturation of hmSpVOs

To benefit the long-term development of hmSpVOs, particularly to facilitate the growth of projecting axons, we prepared hmSpVO sections of 300 μm and cultured them at an air-liquid interface. Cryosection and immunostaining revealed that 3-month-old hmSpVOs cultured at the air-liquid interface contained LMX1B$^+$ and PAX2$^+$ cells, representing the development of both excitatory and inhibitory lineages, respectively (Figures 3A and 3B), consistent with earlier stages (Figures 1G–1K and 2A). Quantification in long-term cultured hmSpVOs derived from multiple hPSC lines (i.e., H9 and H1 hESCs and RC01001A hiPSCs) revealed a similar presence of PAX2$^+$ and LMX1B$^+$ cells (Figure 3C). To understand the structure of intact hmSpVOs, we performed whole-mount staining, which revealed that hmSpVOs exhibited abundant axonal and dendritic processes after long-term culture of more than 4 months (Figure 3D). Notably, NF$^+$ axons exhibited patterned organization adjacent to organoid edges, eventually forming a coalesced NF$^+$ axonal pathway devoid of MAP2$^+$ dendritic process (Figure 3D). Away from organoid edges, both MAP2$^+$ dendrites and NF$^+$ axons displayed a random spatial organization (Figure 3E). Quantifying hmSpVOs at different stages showed that this edge-enriched axonal pathway appeared after a longer culture (i.e., over 120 days) (Figures 3F and 3G). Like H9 hESC-derived hmSpVOs, organoids derived from other hPSC lines (e.g., H1 hESCs and RC01001A hiPSCs) similarly developed edge-enriched axonal pathways after long-term culture (Figures 3H and S4A). These results suggest that hmSpVO cells possess the potential to project axons out of organoids in a coalesced manner, a pattern resembling that of SpV projection neurons in the brain.[27] We also noticed that hThOs cultured under the same condition could develop edge-enriched axonal bundles during long-term culture, whereas in hThOs the NF$^+$ axonal bundles were not uniformly separated from MAP2$^+$ regions as in hmSpVOs (Figures 3F and 3H).

Under this condition, long-term cultured hmSpVOs contained abundant presynaptic vesicle protein synaptophysin (SYP) along NF$^+$ axons (Figure S4B). Viral labeling coupled with staining for the postsynaptic protein postsynaptic density 95 (PSD95) and

(K) Pseudotime heatmap of genes over differentiation pseudotime. Genes are clustered and colored by change over pseudotime.
(L) Heatmap showing transcription factors with high regulatory intensity for each cell type in hmSpVOs.
(M) The proportion of cells positive for marker genes in different types of brain organoids.
See also Figure S3.

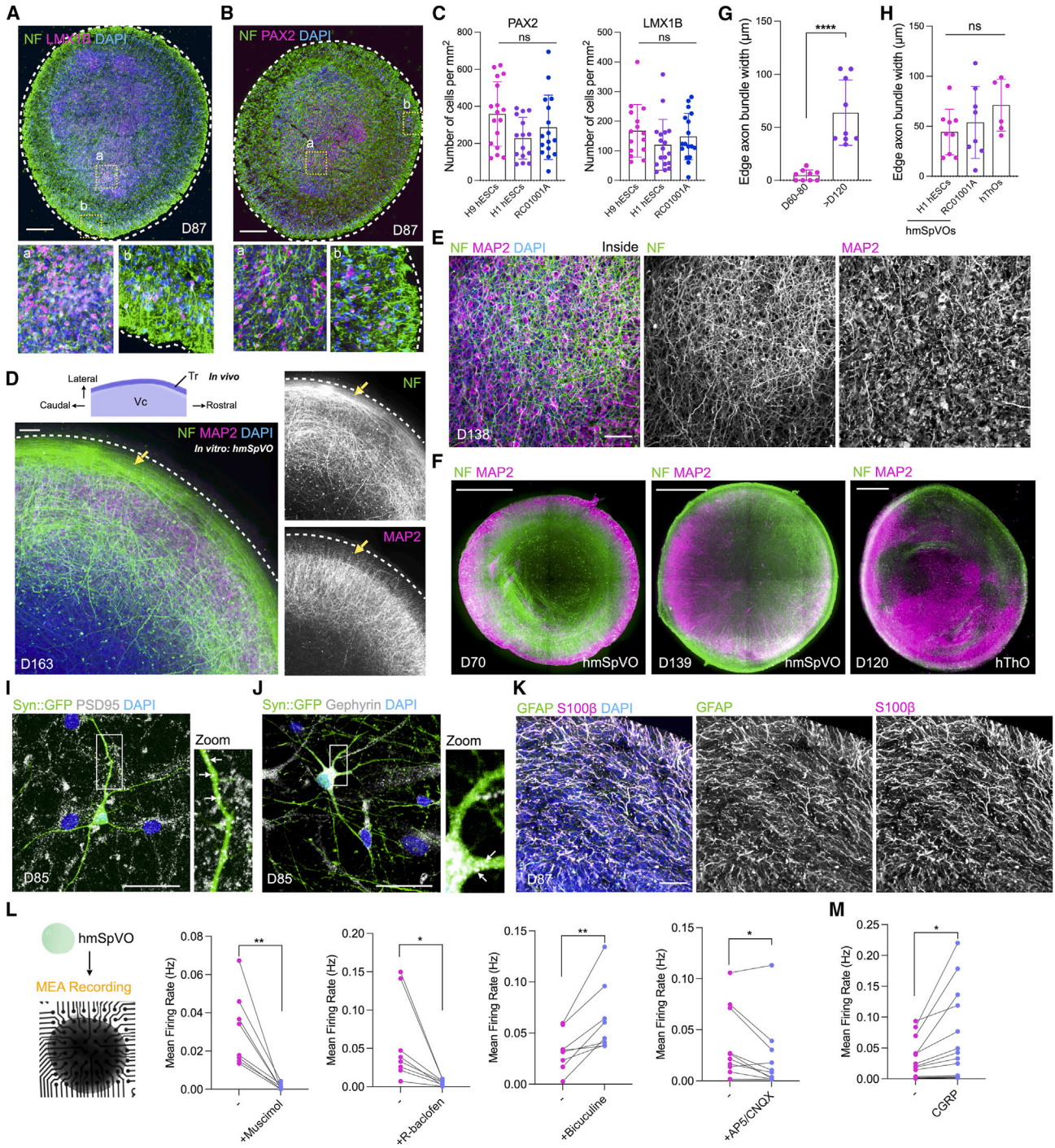

Figure 3. Structure and functional development in hmSpVOs

(A and B) Immunostaining for NF and LMX1B (A), NF and PAX2 (B) in hmSpVOs.

(C) Quantification of PAX2$^+$ and LMX1B$^+$ cells in hmSpVOs (>day 120) derived from different hPSC lines. Data represent the mean ± SD (n = 9, 9, and 9 organoids from 3 batches for H9 hESC-, H1 hESC-, RC01001A hiPSC-derived hmSpVOs, respectively; 1–2 random slices were quantified for each organoid). Multiple comparison analysis testing with ANOVA was used for statistical analysis.

(D) Immunostaining of long-term cultured hmSpVOs for NF and MAP2. Arrows show the region containing coalesced NF$^+$ axons but devoid of MAP2$^+$ dendrites. Tr, spinal trigeminal tract.

(E) Immunostaining of NF and MAP2 in long-term cultured hmSpVOs.

(F) Immunostaining of NF and MAP2 in hmSpVOs from different developmental stages and in hThOs.

(G) Quantification of edge axon bundle width in hmSpVOs at different stages (days 60–80 and days over 120). Data represent the mean ± SD (n = 9 organoids from 3 batches of H9 hESC-derived hmSpVOs). Unpaired two-tail Student's t test was used for comparison. ****$p < 0.0001$.

(legend continued on next page)

the inhibitory postsynaptic protein gephyrin in cells plated from hmSpVOs suggested the development of synapses in differentiated neurons (Figures 3I and 3J). Besides neurons, abundant GFAP$^+$ astrocytes were also produced in hmSpVOs, which closely intermingled with the NF$^+$ neuronal process (Figure S4C). The astrocyte identity of GFAP$^+$ cells was further validated through co-staining for S100β (Figure 3K). We also noticed that the production of astrocytes occurred only after a longer culture (e.g., ~3 months), in accordance with the absence of astrocytes in our scRNA-seq analysis of earlier samples (Figure 2A) and reflecting the fact that neurogenesis precedes astrogenesis during brain development.

To evaluate the electrophysiological activity of hmSpVOs, we performed extracellular recordings using a multi-electrode array (MEA) system (Figure 3L). Although the MEA recorded spontaneous electrical activities in 5-month-old hmSpVOs, pharmacological interventions of hmSpVOs with GABA receptor agonists (muscimol, GABA A receptor agonist; R-baclofen, GABA B receptor agonist) or glutamate receptor antagonists (AP5, N-methyl-D-aspartate [NMDA] receptor; CNQX, Alpha-amino-3-hydroxy-5-methyl-4-isoxazolepropionic acid [AMPA]/kainate receptor) significantly reduced the spike events in hmSpVOs; in contrast, blockade of GABAergic transmission by bicuculline significantly increased spike events (Figures 3L and S4D), suggesting the presence of both GABAergic and glutamatergic neurotransmission in hmSpVOs. Further, given that SpV neurons in the brain can respond to neuropeptides released from peripheral sensory neurons, we stimulated hmSpVOs with calcitonin gene-related peptide (CGRP), a key neuropeptide involved in sensory processing, including nociception.[28] Indeed, MEA recording showed that CGRP treatment significantly increased the spike events in hmSpVOs (Figures 3M and S4E). Overall, these results demonstrate that hmSpVOs can establish structural and functional maturation during development.

Fusion of hmSpVOs and hThOs models trigeminothalamic projections

As an essential sensory relay center in the brain, the SpV receives sensory information, including nociception, from outside the brain and relays the information to the thalamus through the trigeminothalamic tract. The generation of hmSpVOs and our previously established hThOs thus allows for the construction of this brain-nucleus-specific neural circuits *in vitro*. To this end, we fused hmSpVO and hThO sections at an air-liquid interface to produce hSTOs (Figure 4A). To facilitate visualization of axon projection, we inserted a ubiquitous mCherry or GFP expression cassette into the AAVS1 locus of hESCs (Figure S4F). Live imaging of hSTOs prepared through the fusion of mCherry$^+$ hmSpVOs with non-labeled hThOs revealed a robust projection of mCherry$^+$ processes from hmSpVO cells into the hThO region (Figure 4B). Previously, our fusion of hThOs with hCOs recapitulated thalamic projections into the cortical area.[12] To understand the projection events between hmSpVOs and hThOs, we fused mCherry$^+$ hmSpVOs with GFP$^+$ hThOs. Interestingly, we found that mCherry$^+$ hmSpVO-derived bundles of axonal projection into hThO were more robustly observed than GFP$^+$ hThO-derived projection bundles into hmSpVO, and this biased projection pattern was evident even if hmSpVOs and hThOs were fused in a disproportional manner, i.e., hThO with a larger size eventually encapsulated the smaller hmSpVO; in this scenario, GFP$^+$ projection bundles from hThO cells to the hmSpVO region were still less apparent than mCherry$^+$ hmSpVO-to-hThO projection bundles (Figure S4G). To understand projection features, we included different combinations of organoid fusion. Cryosection and immunostaining of fused organoids again revealed that hmSpVOs readily projected axonal bundles to hThOs, which was more robust than projecting to hCOs; in contrast, axon coalescence in hThO-to-hmSpVO direction was not as robust as in hmSpVO-to-hThO direction, unlike the thalamocortical projection when hThOs were fused with hCOs (Figures 4C and S4G).[12] We quantified the axonal projections in cryosections of different fusion conditions. The results revealed that (1) projections from hmSpVO-to-hThO increased over time after fusion (Figure 4D); (2) hmSpVO projection events toward hThO were significantly higher than toward hCO, in both projection coverage and the maximum width of projected axon bundles (Figures 4D and 4E); and (3) although hThOs showed axon growth to hmSpVOs, the sizes of the coalesced axonal pathway were significantly smaller than hmSpVO-to-hThO projections and hThO-to-hCO projections (Figures 4D and 4E). Thus, the axon projection pattern may depend on the type of conjoined neural tissues in fused brain organoids. *In vivo*, the neural circuits between the SpV and thalamus are mainly composed of the trigeminothalamic tract, not vice versa.[25,29] Our results demonstrate that, in the human brain organoid model, SpV-derived neurons exhibit a stronger tendency to project axons coalesced to the conjoined thalamic area than the capability of thalamic neurons to project into the SpV area.

Besides the typical feature that hmSpVO-derived axons near and away from the fusion border coalesced into bundles when projecting into the thalamic side (Figures 4C, 4F, and S4G), we also found that inside hThOs, hmSpVO-originated axons could form projecting pathways with a clear exclusion of soma (Figure S4H). These projection features corroborated our

(H) Quantification of edge axon bundle width in long-term cultured (>120 days) hmSpVOs derived from different hPSC lines and in hThOs. Data represent the mean ± SD (n = 9 and 8 organoids from 3 batches for H1 hESC- and RC01001A hiPSC-derived hmSpVOs, respectively; n = 6 organoids from 3 batches for hThOs derived from H9 hESCs). Multiple comparison analysis testing with ANOVA was used for comparison.
(I and J) Syn::GFP viral labeling of cells plated from hmSpVOs and immunostaining for PSD95 (I) and gephyrin (J).
(K) Immunostaining of hmSpVOs for GFAP and S100β.
(L) MEA-recorded mean firing rates in 5-month-old hmSpVOs before and after pharmacological treatment (n = 8 organoids from 3 batches for muscimol, R-baclofen, or bicuculline treatment; n = 10 organoids from 3 batches for AP5/CNQX treatment). Paired two-tail Student's t test was used for comparison. $^*p < 0.05$, $^{**}p < 0.01$.
(M) MEA-recorded mean firing rates in 5-month-old hmSpVOs before and after CGRP treatment (n = 14 organoids from 3 batches). Paired two-tail Student's t test was used for comparison. $^*p < 0.05$.
Scale bars: 200 μm in (A) and (B); 500 μm in (F); and 50 μm in (D), (E), and (I)–(K).
See also Figure S4.

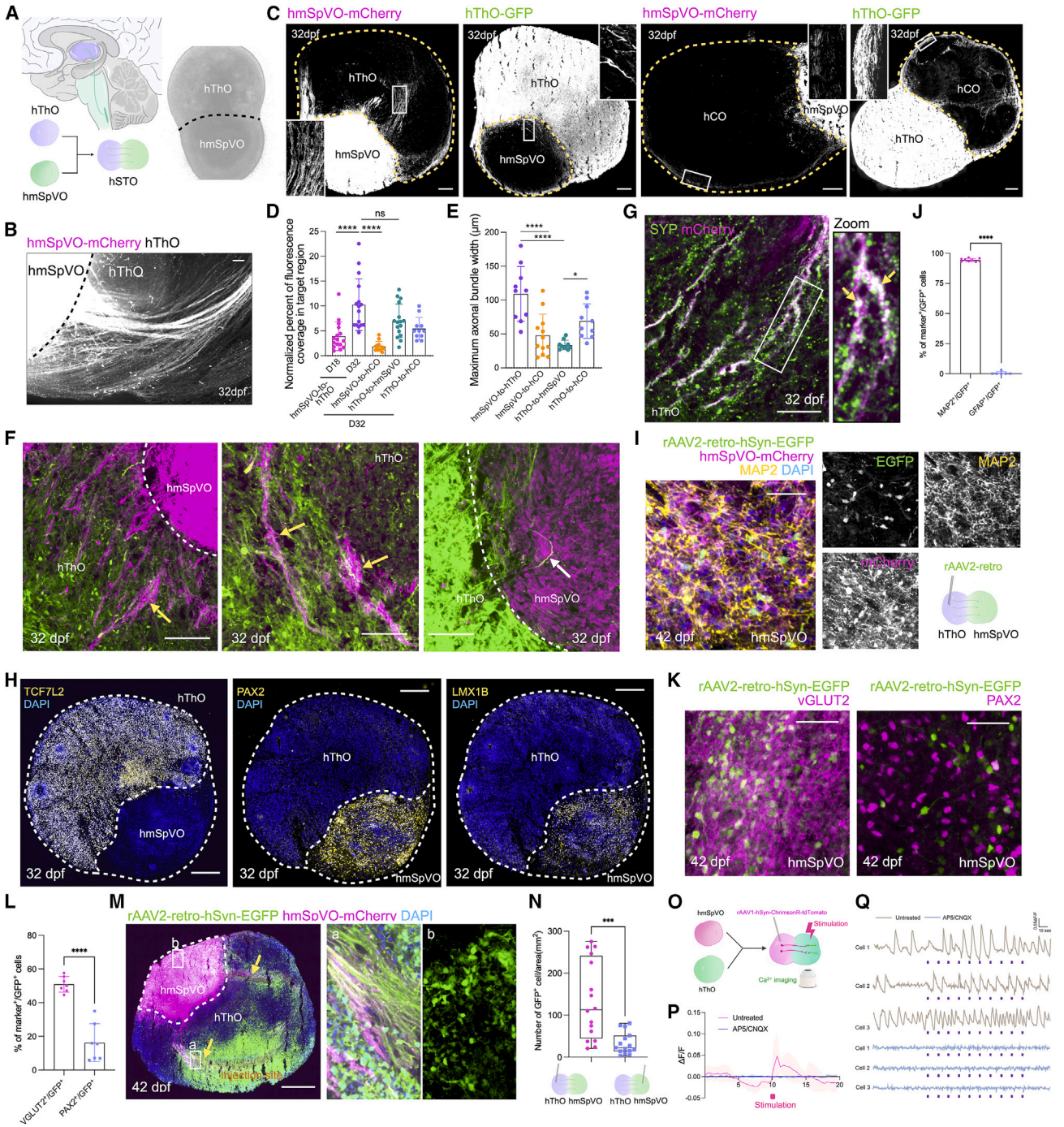

Figure 4. hSTOs model connections between the SpV and thalamus

(A) Schematic view of axon connections between the SpV and thalamus in the brain (top left), the strategy to construct the connection with hSTOs (bottom left), and representative bright-field image of hSTOs (right).

(B) 3D confocal live imaging showing mCherry$^+$ trigeminothalamic projections in an intact hSTO.

(C) Confocal imaging of cryosectioned samples showing the axonal projection events in different fusion combinations.

(D) Normalized percent of fluorescence coverage in the target regions in fused brain organoids. hSTOs were quantified at days 18 and 32 post-fusion. For other fusions, samples at day 32 post-fusion were quantified. Data represent the mean ± SD (hmSpVO-to-hThO-D18: $n = 9$ fused organoids; hmSpVO-to-hThO-D32: $n = 7$ fused organoids; hThO-to-hmSpVO: $n = 7$ fused organoids; hmSpVO-to-hCO: $n = 6$ fused organoids, hThO-to-hCO: $n = 6$ fused organoids; all samples were collected from 3 batches, and 1–2 random slices were quantified for each organoid). Multiple comparison analysis testing with ANOVA was used for comparison. ****$p < 0.0001$.

(legend continued on next page)

observation that hmSpVO neurons tended to form a coalesced axonal pathway near organoid edges when cultured alone (Figures 3D and 3F) and resembled the features of *in vivo* spinal trigeminal tracts.[27] Besides large projection bundles, smaller branches of hmSpVO projections also formed inside hThOs (Figure S4I), suggesting a robust innervation of thalamic cells. Immunostaining for SYP revealed that in hThOs, mCherry$^+$ hmSpVO-derived projections contained SYP$^+$ puncta (Figure 4G), indicating the presence of synaptogenesis during trigeminothalamic targeting. Anterograde tracing[30] in hSTOs from the SpV to the thalamic side revealed that TCF7L2$^+$ thalamic neurons in hThOs were postsynaptic to hmSpVO neurons (Figure S4J). Further, we examined the maintenance of brain region identities in hSTOs by staining for thalamic- and SpV-specific markers. We found that after long-term culture, i.e., around 1 month after organoid fusion, in hSTOs, the thalamic side was enriched with TCF7L2$^+$ thalamic cells, while the hmSpVO side was enriched with PAX2$^+$ and LMX1B$^+$ SpV cells (Figure 4H). These results demonstrate that hSTOs can maintain two distinct brain-region-specific identities during development.

To further examine the connections between the SpV and thalamic cells in hSTOs, we applied retrograde tracing using the rAAV2-retro variant.[31] Microinjection of the rAAV2-retro-hSyn-EGFP vector into the thalamic region readily traced cells in the hmSpVO side (Figure 4I). The retrogradely labeled GFP$^+$ hmSpVO cells mainly expressed the neuronal marker MAP2 but not the astrocyte marker GFAP (Figure 4J). The major population of neurons projecting into the hThO was vGLUT2$^+$ ExNs (50.9% of GFP$^+$ cells) rather than PAX2$^+$ InNs (16.3% of GFP$^+$ cells) (Figures 4K and 4L). These results aligned with the *in vivo* observation that trigeminothalamic projections mainly originate from vGLUT2$^+$ neurons.[25] Notably, retrograde tracing not only labeled hmSpVO cells distant from the vector injection site but also traced the coalesced hmSpVO-derived mCherry$^+$ axonal pathway inside hThOs (Figure 4M). Further, we quantified retrogradely traced cells when the rAAV2-retro-hSyn-EGFP vector was microinjected into either hThOs or hmSpVOs. We found that hThO-to-hmSpVO tracing yielded a significantly higher number of GFP$^+$ cells compared with hmSpVO-to-hThO tracing (Figure 4N), again validating that the axon projection tract was biased as trigeminothalamic rather than thalamotrigeminal (Figures 4C–4F and S4G). To further understand whether neurons in hmSpVOs and hThOs established axon projections, we microinjected AAV1-hSyn-ChrimsonR-tdTomato into the SpV side of hSTOs to express the light-sensitive opsin ChrimsonR in SpV neurons. Optogenetics and calcium imaging were then performed on the thalamic side of hSTOs (Figures 4O and S4K). Applying 561-nm light could elicit calcium responses in thalamic neurons in hThOs (Figures 4P, 4Q, and S4L). We also applied a high-density 3D MEA (HD-MEA), where electrical stimulation was introduced locally in the SpV region of hSTOs through micrometer-scale electrodes (21 × 21 μm in size for each electrode, with 2 adjacent electrodes serving as a positive pole and 2 as a negative pole, separated by one electrode) (Figure S4M). Analysis of the thalamic side showed that electrical stimulation of SpV cells elicited electrical spikes in the thalamic region (Figures S4N and S4O), further suggesting the connections between SpV and thalamic neurons. Taken together, our results show that by fusing hmSpVO and hThO, the trigeminothalamic connections between the human SpV and the thalamus can be recapitulated *in vitro*.

DISCUSSION

Although unguided cerebral organoids, guided region-specific brain organoids, and assembloids have evolved rapidly over the past decade, building brain organoids with nucleus-specific resolutions remains largely unexplored. Developing region-specific brain organoids with nucleus-specific identity is important for human brain modeling at a finer resolution.[16] The medulla of the hindbrain contains different nuclei that are essential for vital body functions, including various sensory and motor

(E) Maximum axonal bundle width in different fusion combinations at day 32 post-fusion. Data represent the mean ± SD (hmSpVO-to-hThO: $n = 6$ fused organoids; hThO-to-hmSpVO: $n = 6$ fused organoids; hmSpVO-to-hCO: $n = 6$ fused organoids; hThO-to-hCO: $n = 6$ fused organoids; all samples were collected from 3 batches, and 1–2 random slices were quantified for each organoid). Multiple comparison analysis testing with ANOVA was used for comparison. $^*p < 0.05$, $^{****}p < 0.0001$.

(F) Confocal imaging of the thalamic side of cryosectioned hSTOs showing both large-size axon bundles and small axon branches (yellow arrow) in trigeminothalamic projections.

(G) Fluorescence images showing the expression of SYP in mCherry$^+$ trigeminothalamic projections.

(H) Immunostaining for TCF7L2, PAX2, and LMX1B in hSTOs generated by fusing mCherry$^+$ hmSpVO and GFP$^+$ hThO.

(I) Immunostaining for MAP2 in rAAV2-retro-hSyn-EGFP retrogradely traced hSTO.

(J) Quantification of MAP2$^+$/GFP$^+$ and GFAP$^+$/GFP$^+$ cells in the hmSpVO side of retrogradely traced hSTOs. Data represent the mean ± SD (MAP2: $n = 9$ and 6 hSTOs from 3 batches for MAP2 and GFAP, respectively; 1 random slice was quantified for each hSTO). Unpaired two-tail Student's t test was used for comparison. $^{****}p < 0.0001$.

(K) Immunostaining of vGLUT2$^+$/GFP$^+$ and PAX2$^+$/GFP$^+$ cells in the hmSpVO side of retrogradely traced hSTOs.

(L) Quantification of vGLUT2$^+$/GFP$^+$ and PAX2$^+$/GFP$^+$ cells in the hmSpVO side of retrogradely traced hSTOs. Data represent the mean ± SD ($n = 7$ hSTOs from 3 batches; 1 random slice was quantified for each hSTO). Unpaired two-tail Student's t test was used for comparison. $^{****}p < 0.0001$.

(M) Fluorescence images showing retrogradely traced hmSpVO cells and hmSpVO-derived axonal pathways in the hThO region.

(N) Quantification of retrogradely traced GFP$^+$ hmSpVO cells and retrogradely traced GFP$^+$ hThO cells ($n = 8$ hSTOs from 3 batches, with 1–2 random slices quantified for each hSTO). Unpaired two-tail Student's t test was used for comparison. $^{***}p < 0.001$.

(O) Schematic showing optogenetic stimulation coupled with calcium imaging in hSTO.

(P) Light-stimulation-triggered average of the calcium response with or without AP5/CNQX ($n = 10$ cells from 4 hSTOs derived from 2 batches). Traces represent the mean and shaded bars represent the SD.

(Q) Representative ΔF/F traces showing spontaneous and light-evoked calcium responses in cells before and after adding AP5 (50 μM) and CNQX (20 μM). Optogenetic stimulations (561 nm, 100 ms each) are indicated with purple rectangles.

Scale bars: 50 μm in (B), (F), (G), (I), and (K); 200 μm in (C); and 500 μm in (H) and (M).

See also Figure S4.

functions and autonomic functions like respiration, heartbeat, and blood pressure. Damage to the medulla leads to severe impairments in body functions.[19] Despite its importance, there has been a lack of brain organoid models to resemble the human medulla, especially to recapitulate defined substructures of the medulla. Here, we focus on the medullary SpV, a critical relay center for nociception. Although SpV abnormality is highly relevant to several neurological diseases, such as trigeminal neuralgia,[32–34] the human model for the SpV and related neural circuits has been unavailable. We have established a region-specific brain organoid model targeting the dorsal domain of the medulla. Importantly, our organoids exhibit an SpV-specific signature. Our study offers an opportunity to investigate medullary SpV development and related brain disorders *in vitro*.

Instead of a complete suspension culture as we established for various other region-specific brain organoids,[8,11–13] here we applied sliced organoid culture at an air-liquid interface[35] for the long-term development of hmSpVOs. Under this strategy, hmSpVOs readily displayed neurogenesis and astrogenesis over months of culture and, notably, exhibited a coalesced pattern of axonal processes, potentially a reminiscence of the spinal trigeminal tract *in vivo*.[27] Because brain-nucleus-like organization features may require long-term development, we anticipate that this air-liquid interface culture strategy could also be beneficial when generating other types of brain-nucleus-specific organoids.

We have also established a system for modeling the connection between the human medullary SpV and thalamus by fusing hmSpVO and hThO. Region-specific brain organoids have enabled the modeling of crosstalk between different regions of the nervous system.[6–10,12] Nevertheless, the modeling of brain-nucleus-specific neural circuits is even more challenging, and no such models have been reported yet. As demonstrated here, brain organoids with nucleus-specific identity can be harnessed to recapitulate human brain-nucleus-related neural circuits in a dish. The biased hmSpVO-to-hThO projection, but not the other way around, suggests a potential intrinsic regulatory mechanism during the development of the trigeminothalamic tract, which deserves further investigation. Overall, we foresee a valuable opportunity to model the human brain nucleus and associated neural circuits using precisely guided, nucleus-specific human brain organoids.

Limitations of the study

The understanding of subnucleus-related features (e.g., Vo, Vi, and Vc) was limited in this study. Future analysis of the human SpV at a single-cell level is needed to demonstrate subnucleus-related signatures of the human brain and guide the design of brain organoid production *in vitro*. Also, the study on the human developing SpV at a single-cell level will improve the understanding of cell types in organoids, especially immature cells (e.g., NPC and IP). Besides, current functional analysis in hSTOs is limited. More functional studies are desired to understand the functionality of neural circuits formed between SpV and thalamic cells in the fusion model and the potential effects of trigeminothalamic connection on the functional maturation of both regions. Further, given the role of the SpV in relaying sensory information, including nociception, to the thalamus and other higher brain structures, it is important to model relevant development or diseases using this system in future studies.

RESOURCE AVAILABILITY

Lead contact

Further information and requests for resources and reagents should be directed to and will be fulfilled by the lead contact, Yangfei Xiang (xiangyf@shanghaitech.edu.cn).

Materials availability

This study did not generate new unique reagents.

Data and code availability

Sequencing data have been deposited in the Gene Expression Omnibus database (GEO: GSE251680) and are publicly available as of publication. The accession numbers for the published datasets analyzed in this paper are listed in the key resources table. This study does not report original algorithms. Any additional information required to reanalyze the data reported in this paper is available from the lead contact upon request.

ACKNOWLEDGMENTS

This study was partly supported by the National Key Research and Development Program of China, China (2021YFF1200800), the National Natural Science Foundation of China, China (32170836), the Central Guidance on Local Science and Technology Development Fund, China (YDZX20233100001002), Shanghai Frontiers Science Center for Biomacromolecules and Precision Medicine at ShanghaiTech University, China, the Shanghai Pujiang Program, China (20PJ1410400), and the ShanghaiTech University start-up fund, China. We thank the facility support from the Molecular Imaging Core and the Molecular and Cell Biology Core at the School of Life Science and Technology, ShanghaiTech University. The HPC Platform of ShanghaiTech University supported computation. We thank the Wei Shen lab at ShanghaiTech University for sharing reagents and the Ji Hu lab at ShanghaiTech University for assisting with neuronal function recording. We also thank Yoshiaki Tanaka at the University of Montreal for assisting with data analysis.

AUTHOR CONTRIBUTIONS

W.P., J.Z., and Y.X. conceived the project and designed experiments. W.P. performed organoid differentiation and characterization experiments. J.Z. performed the analysis of sequencing data. W.Z. and L.J. assisted with organoid differentiation and immunostaining, respectively. X. Zhuang, Y.L., J.W., X.L., Y.Y., and Z.C. performed cell culture and related experiments. W.P., K.Y., and X. Zhu performed functional recordings of organoids. W.P., J.Z., and Y.X. prepared the manuscript.

DECLARATION OF INTERESTS

The authors declare no competing interests.

STAR★METHODS

Detailed methods are provided in the online version of this paper and include the following:

- KEY RESOURCES TABLE
- EXPERIMENTAL MODEL AND STUDY PARTICIPANT DETAILS
  - Cell lines
- METHOD DETAILS
  - Generation of hmSpVOs
  - Generation of hCOs and hThOs
  - Air-liquid interface culture
  - Generation of hSTOs
  - Genome editing
  - Immunofluorescence staining
  - Real-time quantitative PCR (qPCR)

SUPPLEMENTAL INFORMATION

Supplemental information can be found online at https://doi.org/10.1016/j.stem.2024.08.004.

Received: January 10, 2024
Revised: June 16, 2024
Accepted: August 8, 2024
Published: August 28, 2024

REFERENCES

1. Lancaster, M.A., Renner, M., Martin, C.A., Wenzel, D., Bicknell, L.S., Hurles, M.E., Homfray, T., Penninger, J.M., Jackson, A.P., and Knoblich, J.A. (2013). Cerebral organoids model human brain development and microcephaly. Nature *501*, 373–379. https://doi.org/10.1038/nature12517.
2. Kadoshima, T., Sakaguchi, H., Nakano, T., Soen, M., Ando, S., Eiraku, M., and Sasai, Y. (2013). Self-organization of axial polarity, inside-out layer pattern, and species-specific progenitor dynamics in human ES cell-derived neocortex. Proc. Natl. Acad. Sci. USA *110*, 20284–20289. https://doi.org/10.1073/pnas.1315710110.
3. Xiang, Y., Cakir, B., and Park, I.H. (2021). Deconstructing and reconstructing the human brain with regionally specified brain organoids. Semin. Cell Dev. Biol. *111*, 40–51. https://doi.org/10.1016/j.semcdb.2020.05.023.
4. Paşca, A.M., Sloan, S.A., Clarke, L.E., Tian, Y., Makinson, C.D., Huber, N., Kim, C.H., Park, J.Y., O'Rourke, N.A., Nguyen, K.D., et al. (2015). Functional cortical neurons and astrocytes from human pluripotent stem cells in 3D culture. Nat. Methods *12*, 671–678. https://doi.org/10.1038/nmeth.3415.
5. Qian, X.Y., Nguyen, H.N., Song, M.M., Hadiono, C., Ogden, S.C., Hammack, C., Yao, B., Hamersky, G.R., Jacob, F., Zhong, C., et al. (2016). Brain-region-specific organoids using mini-bioreactors for modeling ZIKV exposure. Cell *165*, 1238–1254. https://doi.org/10.1016/j.cell.2016.04.032.
6. Bagley, J.A., Reumann, D., Bian, S., Levi Strauss, J., and Knoblich, J.A. (2017). Fused cerebral organoids model interactions between brain regions. Nat. Methods *14*, 743–751. https://doi.org/10.1038/nmeth.4304.
7. Birey, F., Andersen, J., Makinson, C.D., Islam, S., Wei, W., Huber, N., Fan, H.C., Metzler, K.R.C., Panagiotakos, G., Thom, N., et al. (2017). Assembly of functionally integrated human forebrain spheroids. Nature *545*, 54–59. https://doi.org/10.1038/nature22330.
8. Xiang, Y., Tanaka, Y., Patterson, B., Kang, Y.J., Govindaiah, G., Roselaar, N., Cakir, B., Kim, K.Y., Lombroso, A.P., Hwang, S.M., et al. (2017). Fusion of regionally specified hPSC-derived organoids models human brain development and interneuron migration. Cell Stem Cell *21*, 383–398.e7. https://doi.org/10.1016/j.stem.2017.07.007.
9. Andersen, J., Revah, O., Miura, Y., Thom, N., Amin, N.D., Kelley, K.W., Singh, M., Chen, X., Thete, M.V., Walczak, E.M., et al. (2020). Generation of functional human 3D cortico-motor assembloids. Cell *183*, 1913–1929.e26. https://doi.org/10.1016/j.cell.2020.11.017.
10. Miura, Y., Li, M.Y., Birey, F., Ikeda, K., Revah, O., Thete, M.V., Park, J.Y., Puno, A., Lee, S.H., Porteus, M.H., et al. (2020). Generation of human striatal organoids and cortico-striatal assembloids from human pluripotent stem cells. Nat. Biotechnol. *38*, 1421–1430. https://doi.org/10.1038/s41587-020-00763-w.
11. Cakir, B., Xiang, Y., Tanaka, Y., Kural, M.H., Parent, M., Kang, Y.J., Chapeton, K., Patterson, B., Yuan, Y., He, C.S., et al. (2019). Engineering of human brain organoids with a functional vascular-like system. Nat. Methods *16*, 1169–1175. https://doi.org/10.1038/s41592-019-0586-5.
12. Xiang, Y.F., Tanaka, Y., Cakir, B., Patterson, B., Kim, K.Y., Sun, P.N., Kang, Y.J., Zhong, M., Liu, X.R., Patra, P., et al. (2019). hESC-derived thalamic organoids form reciprocal projections when fused with cortical organoids. Cell Stem Cell *24*, 487–497.e7. https://doi.org/10.1016/j.stem.2018.12.015.
13. Kiral, F.R., Cakir, B., Tanaka, Y., Kim, J., Yang, W.S., Wehbe, F., Kang, Y.J., Zhong, M., Sancer, G., Lee, S.H., et al. (2023). Generation of ventralized human thalamic organoids with thalamic reticular nucleus. Cell Stem Cell *30*, 677–688.e5. https://doi.org/10.1016/j.stem.2023.03.007.
14. Huang, W.K., Wong, S.Z.H., Pather, S.R., Nguyen, P.T.T., Zhang, F., Zhang, D.Y., Zhang, Z., Lu, L., Fang, W., Chen, L., et al. (2021). Generation of hypothalamic arcuate organoids from human induced pluripotent stem cells. Cell Stem Cell *28*, 1657–1670.e10. https://doi.org/10.1016/j.stem.2021.04.006.
15. Tao, Y., Li, X., Dong, Q., Kong, L., Petersen, A.J., Yan, Y., Xu, K., Zima, S., Li, Y., Schmidt, D.K., et al. (2023). Generation of locus coeruleus norepinephrine neurons from human pluripotent stem cells. Nat. Biotechnol. https://doi.org/10.1038/s41587-023-01977-4.
16. Zhang, A., and Wang, Y.L. (2023). Zooming into finer brain structures in vitro. Cell Stem Cell *30*, 503–504. https://doi.org/10.1016/j.stem.2023.04.009.
17. Elkouby, Y.M., and Frank, D. (2010). Wnt/beta-catenin signaling in vertebrate posterior. Colloquium Series on Developmental Biology *1*, 1–79. https://doi.org/10.4199/C00015ED1V01Y201007DEB004.
18. Glover, J.C., Renaud, J.S., and Rijli, F.M. (2006). Retinoic acid and hindbrain patterning. J. Neurobiol. *66*, 705–725. https://doi.org/10.1002/neu.20272.
19. Diek, D., Smidt, M.P., and Mesman, S. (2022). Molecular organization and patterning of the medulla oblongata in health and disease. Int. J. Mol. Sci. *23*. https://doi.org/10.3390/ijms23169260.
20. Sieber, M.A., Storm, R., Martinez-de-La-Torre, M., Müller, T., Wende, H., Reuter, K., Vasyutina, E., and Birchmeier, C. (2007). Lbx1 acts as a selector gene in the fate determination of somatosensory and viscerosensory relay neurons in the hindbrain. J. Neurosci. *27*, 4902–4909. https://doi.org/10.1523/Jneurosci.0717-07.2007.
21. Iskusnykh, I.Y., Steshina, E.Y., and Chizhikov, V.V. (2016). Loss of Ptf1a leads to a widespread cell-fate misspecification in the brainstem, affecting the development of somatosensory and viscerosensory nuclei. J. Neurosci. *36*, 2691–2710. https://doi.org/10.1523/JNEUROSCI.2526-15.2016.
22. Philippidou, P., and Dasen, J.S. (2013). Hox genes: choreographers in neural development, architects of circuit organization. Neuron *80*, 12–34. https://doi.org/10.1016/j.neuron.2013.09.020.
23. Braun, E., Danan-Gotthold, M., Borm, L.E., Lee, K.W., Vinsland, E., Lönnerberg, P., Hu, L., Li, X., He, X., Andrusivová, Ž., et al. (2023). Comprehensive cell atlas of the first-trimester developing human brain. Science *382*, eadf1226. https://doi.org/10.1126/science.adf1226.
24. Fleck, J.S., Sanchís-Calleja, F., He, Z., Santel, M., Boyle, M.J., Camp, J.G., and Treutlein, B. (2021). Resolving organoid brain region identities by mapping single-cell genomic data to reference atlases. Cell Stem Cell *28*, 1177–1180. https://doi.org/10.1016/j.stem.2021.03.015.
25. Zhang, C.K., Li, Z.H., Qiao, Y., Zhang, T., Lu, Y.C., Chen, T., Dong, Y.L., Li, Y.Q., and Li, J.L. (2018). VGLUT1 or VGLUT2 mRNA-positive neurons in spinal trigeminal nucleus provide collateral projections to both the thalamus and the parabrachial nucleus in rats. Mol. Brain *11*, 22. https://doi.org/10.1186/s13041-018-0362-y.

26. García-Guillén, I.M., Martínez-de-la-Torre, M., Puelles, L., Aroca, P., and Marín, F. (2021). Molecular segmentation of the spinal trigeminal nucleus in the adult mouse brain. Front. Neuroanat. *15*, 785840. https://doi.org/10.3389/fnana.2021.785840.

27. Hirahara, M., Fujiwara, N., and Seo, K. (2017). Novel trigeminal slice preparation method for studying mechanisms of nociception transmission. J. Neurosci. Methods *286*, 6–15. https://doi.org/10.1016/j.jneumeth.2017.05.019.

28. Zheng, F., Nixdorf-Bergweiler, B.E., van Brederode, J., Alzheimer, C., and Messlinger, K. (2021). Excitatory effects of calcitonin gene-related peptide (CGRP) on superficial Sp5C neurons in mouse medullary slices. Int. J. Mol. Sci. *22*. https://doi.org/10.3390/ijms22073794.

29. Saito, H., Katagiri, A., Okada, S., Mikuzuki, L., Kubo, A., Suzuki, T., Ohara, K., Lee, J., Gionhaku, N., Iinuma, T., et al. (2017). Ascending projections of nociceptive neurons from trigeminal subnucleus caudalis: A population approach. Exp. Neurol. *293*, 124–136. https://doi.org/10.1016/j.expneurol.2017.03.024.

30. Zingg, B., Chou, X.L., Zhang, Z.G., Mesik, L., Liang, F., Tao, H.W., and Zhang, L.I. (2017). AAV-mediated anterograde transsynaptic tagging: mapping Corticocollicular input-defined neural pathways for defense behaviors. Neuron *93*, 33–47. https://doi.org/10.1016/j.neuron.2016.11.045.

31. Tervo, D.G.R., Hwang, B.Y., Viswanathan, S., Gaj, T., Lavzin, M., Ritola, K.D., Lindo, S., Michael, S., Kuleshova, E., Ojala, D., et al. (2016). A designer AAV variant permits efficient retrograde access to projection neurons. Neuron *92*, 372–382. https://doi.org/10.1016/j.neuron.2016.09.021.

32. Iyengar, S., Ossipov, M.H., and Johnson, K.W. (2017). The role of calcitonin gene-related peptide in peripheral and central pain mechanisms including migraine. Pain *158*, 543–559. https://doi.org/10.1097/j.pain.0000000000000831.

33. Puja, G., Sonkodi, B., and Bardoni, R. (2021). Mechanisms of peripheral and central pain sensitization: focus on ocular pain. Front. Pharmacol. *12*, 764396. https://doi.org/10.3389/fphar.2021.764396.

34. Terrier, L.M., Hadjikhani, N., and Destrieux, C. (2022). The trigeminal pathways. J. Neurol. *269*, 3443–3460. https://doi.org/10.1007/s00415-022-11002-4.

35. Giandomenico, S.L., Mierau, S.B., Gibbons, G.M., Wenger, L.M.D., Masullo, L., Sit, T., Sutcliffe, M., Boulanger, J., Tripodi, M., Derivery, E., et al. (2019). Cerebral organoids at the air-liquid interface generate diverse nerve tracts with functional output. Nat. Neurosci. *22*, 669–679. https://doi.org/10.1038/s41593-019-0350-2.

36. González, F., Zhu, Z., Shi, Z.D., Lelli, K., Verma, N., Li, Q.V., and Huangfu, D. (2014). An iCRISPR platform for rapid, multiplexable, and inducible genome editing in human pluripotent stem cells. Cell Stem Cell *15*, 215–226. https://doi.org/10.1016/j.stem.2014.05.018.

37. Qian, K., Huang, C.T.L., Chen, H., Blackbourn, L.W., Chen, Y., Cao, J., Yao, L., Sauvey, C., Du, Z., and Zhang, S.C. (2014). A simple and efficient system for regulating gene expression in human pluripotent stem cells and derivatives. Stem Cells *32*, 1230–1238. https://doi.org/10.1002/stem.1653.

38. Chen, Y., Xiong, M., Dong, Y., Haberman, A., Cao, J., Liu, H., Zhou, W., and Zhang, S.C. (2016). Chemical control of grafted human PSC-derived neurons in a mouse model of Parkinson's disease. Cell Stem Cell *18*, 817–826. https://doi.org/10.1016/j.stem.2016.03.014.

39. Hao, Y., Hao, S., Andersen-Nissen, E., Mauck, W.M., 3rd, Zheng, S., Butler, A., Lee, M.J., Wilk, A.J., Darby, C., Zager, M., et al. (2021). Integrated analysis of multimodal single-cell data. Cell *184*, 3573–3587.e29. https://doi.org/10.1016/j.cell.2021.04.048.

40. McGinnis, C.S., Murrow, L.M., and Gartner, Z.J. (2019). DoubletFinder: doublet detection in single-cell RNA sequencing data using artificial nearest neighbors. Cell Syst. *8*, 329–337.e4. https://doi.org/10.1016/j.cels.2019.03.003.

41. Van de Sande, B., Flerin, C., Davie, K., De Waegeneer, M., Hulselmans, G., Aibar, S., Seurinck, R., Saelens, W., Cannoodt, R., Rouchon, Q., et al. (2020). A scalable SCENIC workflow for single-cell gene regulatory network analysis. Nat. Protoc. *15*, 2247–2276. https://doi.org/10.1038/s41596-020-0336-2.

42. Korsunsky, I., Millard, N., Fan, J., Slowikowski, K., Zhang, F., Wei, K., Baglaenko, Y., Brenner, M., Loh, P.-R., and Raychaudhuri, S. (2019). Fast, sensitive and accurate integration of single-cell data with Harmony. Nat. Methods *16*, 1289–1296. https://doi.org/10.1038/s41592-019-0619-0.

43. Bergen, V., Lange, M., Peidli, S., Wolf, F.A., and Theis, F.J. (2020). Generalizing RNA velocity to transient cell states through dynamical modeling. Nat. Biotechnol. *38*, 1408–1414. https://doi.org/10.1038/s41587-020-0591-3.

44. Dobin, A., Davis, C.A., Schlesinger, F., Drenkow, J., Zaleski, C., Jha, S., Batut, P., Chaisson, M., and Gingeras, T.R. (2013). STAR: ultrafast universal RNA-seq aligner. Bioinformatics *29*, 15–21. https://doi.org/10.1093/bioinformatics/bts635.

45. Li, B., and Dewey, C.N. (2011). RSEM: accurate transcript quantification from RNA-Seq data with or without a reference genome. BMC Bioinformatics *12*, 323. https://doi.org/10.1186/1471-2105-12-323.

46. Ewels, P.A., Peltzer, A., Fillinger, S., Patel, H., Alneberg, J., Wilm, A., Garcia, M.U., Di Tommaso, P., and Nahnsen, S. (2020). The nf-core framework for community-curated bioinformatics pipelines. Nat. Biotechnol. *38*, 276–278. https://doi.org/10.1038/s41587-020-0439-x.

47. Barbie, D.A., Tamayo, P., Boehm, J.S., Kim, S.Y., Moody, S.E., Dunn, I.F., Schinzel, A.C., Sandy, P., Meylan, E., Scholl, C., et al. (2009). Systematic RNA interference reveals that oncogenic KRAS-driven cancers require TBK1. Nature *462*, 108–112. https://doi.org/10.1038/nature08460.

48. Melé, M., Ferreira, P.G., Reverter, F., DeLuca, D.S., Monlong, J., Sammeth, M., Young, T.R., Goldmann, J.M., Pervouchine, D.D., Sullivan, T.J., et al. (2015). Human genomics. The human transcriptome across tissues and individuals. Science *348*, 660–665. https://doi.org/10.1126/science.aaa0355.

49. Haghverdi, L., Lun, A.T.L., Morgan, M.D., and Marioni, J.C. (2018). Batch effects in single-cell RNA-sequencing data are corrected by matching mutual nearest neighbors. Nat. Biotechnol. *36*, 421–427. https://doi.org/10.1038/nbt.4091.

50. Braun, E., Danan-Gotthold, M., Borm, L.E., Vinsland, E., Lee, K.W., Lönnerberg, P., Hu, L., Li, X., He, X., Andrusivová, Ž., et al. (2022). Comprehensive cell atlas of the first-trimester developing human brain. Preprint at bioRxiv. https://doi.org/10.1101/2022.10.24.513487.

51. Cao, J., Spielmann, M., Qiu, X., Huang, X., Ibrahim, D.M., Hill, A.J., Zhang, F., Mundlos, S., Christiansen, L., Steemers, F.J., et al. (2019). The single-cell transcriptional landscape of mammalian organogenesis. Nature *566*, 496–502. https://doi.org/10.1038/s41586-019-0969-x.

STAR★METHODS

KEY RESOURCES TABLE

REAGENT or RESOURCE	SOURCE	IDENTIFIER
Antibodies		
synaptophysin	Abcam	Cat# ab8049; RRID: AB_2198854
SOX2	Cell signaling	Cat# 3579; RRID: AB_2195767
MAP2	Millipore	Cat# MAB3418; RRID: AB_11212326
MAP2	Abcam	Cat# ab183830; RRID: AB_2895301
Neurofilament	Abcam	Cat# ab7795; RRID: AB_306084
Neurofilament	Millipore	Cat# AB1989, RRID: AB_91202
GFAP	Invitrogen	Cat# 130300; RRID: AB_86543
S-100β	Sigma-merck	Cat# S2532; RRID: AB_477499
NKX2-2	Abcam	Cat# ab191077; RRID: AB_2811076
NKX6-1	Abcam	Cat# ab221549; RRID: AB_2754979
PAX7	Abcam	Cat# ab92317; RRID: AB_10561454
LBX1	Invitrogen	Cat# PA564884; RRID: AB_2662958
LMX1B	Sigma-Aldrich	Cat# HPA073716; RRID: AB_2686630
PAX2	Abcam	Cat# ab150391; RRID: AB_3065222
LHX1/5	Developmental Studies Hybridoma Bank	Cat# 4F2; RRID: AB_531784
TCF7L2	Cell Signaling	Cat# 2569T; RRID: AB_2199816
TBR1	Abcam	Cat# ab31940; RRID: AB_2200219
GABA	Sigma-merck	Cat# A0310; RRID: AB_476667
Gephyrin	Santa Cruz	Cat# sc-25311; RRID: AB_627670
PHOX2B	Santa Cruz	Cat# sc-376997; RRID: AB_2813765
SOX10	R&D	Cat# MAB2864; RRID: AB_2195180
OLIG3	R&D	Cat# MAB2456; RRID: AB_2157678
VGLUT2	Millipore	Cat# MAB5504; RRID: AB_2187552
PSD95	Santa Cruz	Cat# sc-32290; RRID: AB_628114
Bacterial and virus strains		
pAAV-hSyn-EGFP-P2A-3xFLAG-WPRE	OBiO	https://www.obiosh.com/
pAAV-hSyn-EGFP-3XFLAG-WPRE retrograde tracer virus	OBiO	https://www.obiosh.com/
rAAV2/1-hSyn-Cre-WPRE-hGH polyA	BrainVTA	Cat# PT-0136
rAAV2/9-EF1a-DIO-EGFP-WPRE-hGH polyA	BrainVTA	Cat# PT-0795
rAAV2/1-hSyn-ChrimsonR-tdTomato-WPRE-hGH polyA	BrainVTA	Cat# PT-1432
Chemicals, peptides, and recombinant proteins		
mTeSR Plus	Stem Cell Technologies	Cat# 100-0276
DMEM-F12	Life Technologies	Cat# C11330500BT
Neurobasal Media	Life Technologies	Cat# 21103049
BrainPhys Neuronal Medium	stemcell	Cat# 05790
KNOCKOUT(TM) SR	invitrogen	Cat# 10828028
Accutase	Stem Cell Technologies	Cat# 07920
Amino acids, non-essential	Life Technologies	Cat# 11140050
Penicillin/Streptomycin	Life Technologies	Cat# 15140122
Glutamax	Life Technologies	Ca# 35050061
β-Mercaptoethanol	Sigma-Aldrich	Ca# M3148
N2	Life Technologies	Cat# 17502048
B27(-VA)	invitrogen	Cat#12587010

(*Continued on next page*)

Continued

REAGENT or RESOURCE	SOURCE	IDENTIFIER
D- (+)-Glucose solution (45% H_2O)	Sigma-Aldrich	Cat# G8769
B27	Life Technologies	Cat# 17504044
Insulin	Beyotime	Cat# P3376
EGF	novoprotein	Cat#C029B
Retinoic acid (RA)	Sigma-Aldrich	Cat# R2625
NGF	novoprotein	Cat# C060
Matrigel	BD	Cat# 354230
Y-27632	MCE	Cat# HY-10583
LDN193189	MCE	Cat# HY-12071A
SB431542	Abcam	Cat# ab120163
CHIR99021	Stem Cell Technologies	Cat# 72054
XAV939	Sigma-Aldrich	Cat# X3004
PD325901	Selleck	Cat# S1036
Purmorphamine	stemcell	Cat# D204
BMP4	Abcam	Cat# ab238298
SHH	R&D	Cat# 464-SH-200
BDNF	novoprotein	Cat# C076
Bucladesine sodium	MCE	Cat# HY-B0764
Ascorbic acid	Sigma-Aldrich	Cat# A92902
O.C.T compound	Tissue-Tek	Cat# 4583
Bovine serum albumin	Sangong	Cat# A500023-0100
Triton X-100	Sigma-Aldrich	Cat# T8787
DAPI	Solarbio	Cat# C0065
Agarose, low gelling temperature	Sigma-Aldrich	Cat# A9414
ProLong Gold Antifade Reagent	ThermoFisher	Cat# P36930
Muscimol	MCE	Cat# HY-N2313
(R)-Baclofen	MCE	Cat# HY-17354
Bicuculline	MCE	Cat# HY-N0219
D-AP5	MCE	Cat# HY-100714A
CNQX disodium salt	Tocris	Cat# 1045
α-CGRP (human)	MCE	Cat# HY-P1071
Cal-520	AAT Bioquest	Cat# 21130
powerload	Invitrogen	Cat# P10020
Critical commercial assays		
FastPure Cell/Tissue Total RNA Isolation Kit	Vazyme	Cat# RC101
HiScript III All-in-one RT SuperMix Perfect	Vazyme	Cat# R333
Taq Pro Universal SYBR qPCR Master Mix	Vazyme	Cat# Q712
RapiClear	Sunjin lab	Cat# RC152001
Deposited data		
Raw and processed RNA-seq and scRNA-seq	This paper	GEO: GSE251680
RNA-seq for hESC and hCO and scRNA-seq for hCO	Xiang et al.[8]	GEO: GSE97882
scRNA-seq for hThO	Xiang et al.[12]	GEO: GSE122342
Reference transcriptome GRCh38	10X genomics	https://support.10xgenomics.com/
Microarray dataset for human medulla	Allen brain	https://human.brain-map.org/
scRNA-seq for developing human brain	Braun et al.[23]	https://github.com/linnarsson-lab/developing-human-brain/
Experimental models: Cell lines		
H9 hESC line	WiCell	https://www.ncbi.nlm.nih.gov/pubmed/9804556/

(*Continued on next page*)

Continued

REAGENT or RESOURCE	SOURCE	IDENTIFIER
H1 hESC line	WiCell	https://www.ncbi.nlm.nih.gov/pubmed/9804556/
hiPSCs RC01001A line	Nuwacell	https://www.nuwacell.com/
hiPSC RC01001B line	Nuwacell	https://www.nuwacell.com/
H9-AAVS1-CAG-GFP hESC line	This paper	N/A
H9-AAVS1-CAG-mCherry hESC line	This paper	N/A
Recombinant DNA and virus		
AAVS1-TALEN-L	Gonzalez et al.[36]	Addgene # 59025
AAVS1-TALEN-R	Gonzalez et al.[36]	Addgene # 59026
AAVS1-CAG-hrGFP	Qian et al.[37]	Addgene # 52344
AAVS1-CAG-mCherry	Chen et al.[38]	Addgene # 80946
Software and algorithms		
Maestro pro MEA system	Axion Biosystems	https://www.axionbiosystems.com/
Plexon Offline Sorter	Plexon	https://plexon.com/products/offline-sorter/
AxIS Navigator	Axion Biosystems	https://www.axionbiosystems.com/
Neural Metric Tool	Axion Biosystems	https://www.axionbiosystems.com/
Fiji	N/A	https://fiji.sc
BioCAM DupleX	3Brain	https://www.3brain.com/products/single-well/biocam-duplex
Brainwave5	3Brain	https://www.3brain.com/products/software/brainwave5
nf-core/rnaseq pipeline (v3.13.2)	N/A	https://github.com/nf-core/rnaseq
STAR (v2.7.10a)	N/A	https://github.com/alexdobin/STAR
RSEM (v1.3.1)	N/A	https://github.com/deweylab/RSEM
GSVA (1.44.5)	N/A	https://github.com/rcastelo/GSVA
Voxhunt (v 1.0.1)	Fleck et al.[24]	https://github.com/quadbio/VoxHunt
Cell Ranger (v6.1.2)	N/A	https://www.10xgenomics.com/support/software/cell-ranger
Seurat (v 4.3.0)	Hao et al.[39]	https://satijalab.org/seurat/
DoubletFinder (v 2.0.3)	McGinnis et al.[40]	https://github.com/chris-mcginnis-ucsf/DoubletFinder
SeuratWrappers (v 0.3.1)	N/A	https://github.com/satijalab/seurat-wrappers
AUCell (v 1.18.1)	N/A	https://github.com/aertslab/AUCell
SCENIC (v 1.3.1)	Sande et al.[41]	https://github.com/aertslab/SCENIC
Harmony (v 0.1.1)	Korsunsky et al.[42]	https://github.com/immunogenomics/harmony
scvelo (v0.2.5)	Bergen et al.[43]	https://github.com/theislab/scvelo
Other		
Orbital shaker	IKA	KS260
Nucleofector	Lonza	AAB-1001
Micropipette Puller	RWD	MP-500
Glass microelectrode injection pump	RWD	R480
U-bottom ultra-low-attachment 96-well plate	Corning	CLS7007-24EA
Tissue Culture Plate Insert 3.0um	BIOFIL	TCS002006
Ultra-low-attachment 6-well plate	BIOFIL	TCP030006
CytoView MEA plate (six-well)	Axion Biosystems	M384-tMEA-6W

EXPERIMENTAL MODEL AND STUDY PARTICIPANT DETAILS

Cell lines

Female H9 hESCs, male H1 hESCs, male hiPSCs RC01001A, female hiPSC RC01001B, and all derivative clones from genome manipulation (H9-AAVS1-CAG-GFP hESCs and H9-AAVS1-CAG-mCherry hESCs) were cultured on Matrigel-coated tissue culture

dish with mTeSR plus media in a humidified 37°C incubator with 5% CO_2. hESC lines H9 and H1 were commercially available from WiCell, and hiPSC lines RC01001A and RC01001B were commercially available from Nuwacell (see key resources table). RC01001A and RC01001B were derived from the peripheral blood mononuclear cells of a 36-year-old male and the umbilical cord cells of a newborn female through Sendai virus vector-mediated reprogramming, respectively. The identities of H9-AAVS1-CAG-GFP hESCs and H9-AAVS1-CAG-mCherry hESCs can be verified by constitutive expressions of GFP and mCherry proteins driven by the CAG promoter, respectively. hPSCs were passaged every 4-5 days by 0.5 mM EDTA treatment (pH 8.0). All experiments involving hESCs and hiPSCs were approved by the ShanghaiTech Research Ethics Committee.

METHOD DETAILS

Generation of hmSpVOs

On day 0, feeder-free hESC colonies were dissociated into single cells using Accutase treatment for 10 minutes. Single cells re-suspended in induction media (DMEM-F12, 15% (v/v) KSR, 1% (v/v) MEM-NEAA, 1% (v/v) Glutamax, and 100 μM β-Mercaptoethanol) supplemented with 100 nM LDN193189, 10 μM SB431542, 3 μM CHIR99021, and 50 μM Y27632 were plated to ultra-low attachment 96-well plate (1500 cells/well). On day 2, all media were replaced with the induction media supplemented with 100 nM LDN193189, 10 μM SB431542, 3 μM CHIR99021, and 100 nM retinoic acid (RA). On days 4 and 6, the above-mentioned media were replenished. On day 8, organoids were transferred to a spinning culture (80 rpm/min) in ultra-low attachment 6 well plates (8-12 organoids/well). The media was changed to differentiation media (1:1 mixture of DMEM-F12 and Neurobasal media, 0.5% (v/v) N2 supplement, 1% (v/v) B27 supplement, 0.5% (v/v) MEM-NEAA, 1% (v/v) Glutamax, 2.5 μg/mL Insulin, 50 μM β-Mercaptoethanol, and 1% (v/v) Penicillin/Streptomycin), supplemented with 3 μM CHIR99021, 10 ng/ml EGF and 20 ng/ml NGF. The media was replenished every other day. On days 12 and 14, dissolved Matrigel (1%, v/v) was added. Beginning at day 16, differentiation media (1:1 mixture of DMEM-F12 and Neurobasal media, 0.5% (v/v) N2 supplement, 1% (v/v) B27 supplement, 0.5% (v/v) MEM-NEAA, 1% (v/v) Glutamax, 2.5 μg/mL Insulin, 50 μM β-Mercaptoethanol, and 1% (v/v) Penicillin/Streptomycin) supplemented with 20 ng/ml BDNF and 200 μM ascorbic acid was used. Media was replenished every other day before day 30 and every four days thereafter.

Generation of hCOs and hThOs

hCOs and hThOs were generated as previously described.[8,12] Briefly, for hCOs generation, single-cell suspensions from hESCs were plated to ultra-low attachment 96-well plate (9000 cells/well) in induction media (DMEM-F12, 15% (v/v) KSR, 1% (v/v) MEM-NEAA, 1% (v/v) Glutamax, and 100 μM β-Mercaptoethanol) supplemented with 100 nM LDN193189, 10 μM SB431542, 2 μM XAV939, and 50 μM Y27632. The above-mentioned media was replenished every other day until day 10 (on day 4, Y27632 was removed). Organoids were transferred to a spinning culture (80 rpm/min) in ultra-low attachment 6-well plates beginning at day 10 (6-8 organoids/well). Differentiation media without vitamin A (1:1 mixture of DMEM-F12 and Neurobasal media, 0.5% (v/v) N2 supplement, 1% (v/v) B27 supplement minus vitamin A, 0.5% (v/v) MEM-NEAA, 1% (v/v) Glutamax, 2.5 μg/mL Insulin, 50 μM β-Mercaptoethanol and 1% (v/v) Penicillin/Streptomycin) was used from day 10 to day 18 (media replenished every other day). Since day 18, differentiation media with vitamin A (1:1 mixture of DMEM-F12 and Neurobasal media, 0.5% (v/v) N2 supplement, 1% (v/v) B27 supplement, 0.5% (v/v) MEM-NEAA, 1% (v/v) Glutamax, 2.5 μg/mL Insulin, 50 μM β-Mercaptoethanol, and 1% (v/v) Penicillin/Streptomycin) supplemented with 20 ng/ml BDNF and 200 μM ascorbic acid was used (media replenished every other day before day 25, and every four days thereafter).

For hThOs generation, single-cell suspensions from hESCs were plated to ultra-low attachment 96-well plate (20000 cells/well) in induction media (DMEM-F12, 15% (v/v) KSR, 1% (v/v) MEM-NEAA, 1% (v/v) Glutamax, and 100 μM β-Mercaptoethanol) supplemented with 100 nM LDN193189, 10 μM SB431542, 4 μg/ml Insulin and 50 μM Y27632. The above-mentioned media was replenished every other day until day 8 (on day 4, Y27632 was removed). On day 8, organoids were transferred to spinning culture (80 rpm/min) in ultra-low attachment 6 well plates (8-12 organoid/well). From day 8 to day 16, patterning media (DMEM-F12, 0.15% (w/v) Dextrose, 100 μM β-Mercaptoethanol, 1% (v/v) N2 supplement, and 2% (v/v) B27 supplement minus vitamin A) supplemented with 30 ng/ml BMP7 and 1 μM PD325901 was used (media replenished every other day). Beginning at day 16, differentiation media (1:1 mixture of DMEM-F12 and Neurobasal media, 0.5% (v/v) N2 supplement, 1% (v/v) B27 supplement, 0.5% (v/v) MEM-NEAA, 1% (v/v) Glutamax, 2.5 μg/mL Insulin, 50 μM β-Mercaptoethanol, and 1% (v/v) Penicillin/Streptomycin) supplemented with 20 ng/ml BDNF and 200 μM ascorbic acid was used. Media was replenished every other day before day 25 and every four days thereafter.

Air-liquid interface culture

For culture at an air-liquid interface, hmSpVOs at days 25-30 were gently collected using a cut plastic pipette tip without disturbing the organoid structure and embedded in 3% low-gelling-temperature agarose in an embedding mold. Typically, 3-6 hmSpVOs were embedded per mold. The agarose blocks containing organoids were sectioned using a vibrating microtome in 1× PBS (without Ca^{2+} and Mg^{2+}). Organoid sections (300 μm-thick) were transferred onto cell culture inserts in transwell plates (6-well format). Differentiation media (1:1 mixture of DMEM-F12 and Neurobasal media, 0.5% (v/v) N2 supplement, 1% (v/v) B27 supplement, 0.5% (v/v) MEM-NEAA, 1% (v/v) Glutamax, 2.5 μg/mL Insulin, 50 μM β-Mercaptoethanol, and 1% (v/v) Penicillin/Streptomycin) supplemented with 20 ng/ml BDNF and 200 μM ascorbic acid was added and kept below the culture insert to ensure organoid sections remained at

the air-liquid interface. Organoid sections were kept in stationary culture for one day to recover and then transferred onto an orbital shaker for long-term culture at 37°C with 5% CO_2. Media was changed every other day.

Generation of hSTOs

To generate hSTOs, day 25-30 hmSpVO and hThO were prepared, and 300 μm-thick organoid sections were prepared as described above. A single hmSpVO section and single hThO section were transferred onto the transwell insert of a 6-well plate and placed adjacent to each other to allow spontaneous fusion of the two samples, referred to as hSTOs. Differentiation media (as in the air-liquid culture described above) was added and kept below the transwell insert to establish a culture at the air-liquid interface and to avoid the movement of organoid sections. The newly prepared hSTOs were incubated for one day without shaking and then transferred onto an orbital shaker for long-term culture at 37°C with 5% CO_2. Media was changed every other day.

Genome editing

For the generation of H9-AAVS1-CAG-GFP hESCs and H9-AAVS1-CAG-mCherry hESCs reporter lines, 2×10^6 single cells dissociated from H9 hESCs were electroporated with 1 μg of AAVS1-TALEN-L plasmid, 1 μg of AAVS1-TALEN-R plasmid, and 8 μg of donor plasmids (either AAVS1-CAG-GFP or AAVS1-CAG-mCherry plasmid), and then plated onto Matrigel-coated plate. Three days after electroporation, cells were treated with puromycin for 1 week and allowed for recovery for another 5∼7 days. Then, GFP^+ or $mCherry^+$ clones were picked and expanded.

Immunofluorescence staining

Organoids were fixed in 4% PFA at 4°C for 1-2 days, washed 3 times with PBS (10 min RT incubation for each wash), and incubated in 30% sucrose solution at 4°C for 2 days. Organoids were then incubated in O.C.T compound at RT for 15 min, transferred to tissue base molds, and embedded in O.C.T compound. Embedded organoids were stored at -80°C or immediately used for cryosectioning (30-50 μm slices). Slices were incubated with 0.3% Triton-100 at RT for 15 min, blocked with 3% BSA/PBS at RT for 2 h, and incubated with primary antibody diluted in 3% BSA/PBS at 4°C overnight. After three times PBS washes, slices were incubated with secondary antibody diluted in 3% BSA/PBS at RT for 1 h, then washed three times with PBS wash, stained by DAPI for 15 min, and mounted. A list of antibodies is provided in the key resources table.

For whole-mount staining, organoids were processed using the RapiClear Solution. Briefly, 4% PFA fixed organoids were treated with 2% PBST (2% Triton X-100 in PBS) for 1 day at 4°C, then washed with PBS three times (15 min/time at RT). Samples were kept in a 1.5 mL tube filled with freshly prepared blocking buffer (3% normal goat serum and 0.3% PBST (0.3%Triton-X100 in PBS) at 4°C for 1 day. Then, organoids were incubated with the primary antibody in a 1.5 mL tube filled with the blocking buffer on an orbital shaker at 4°C for 2 days. After washing with PBS three times (1 h/time at RT), organoids were kept in PBS at 4°C overnight. Then, organoids were incubated with the secondary antibody in a 1.5 mL tube filled with the blocking buffer at 4°C for 2 days. After three washes with PBS (1 h/time at RT), organoids were kept in PBS at 4°C overnight. After another three washes with PBS (20 min/time at RT), samples were incubated in a 1.5 mL tube filled with DAPI solution (1:1000 dilution in blocking buffer) at 4°C overnight. After three washes with PBS (1 h/time at RT), organoids were transferred to the bottom of the glass dish, and RapiClear was added at RT for 2-3 hours. For all the immunostaining experiments, fluorescent images were captured by a Nikon CSU-W1 Sora 2Camera microscope and analyzed using the ImageJ software.

Real-time quantitative PCR (qPCR)

Organoids for each group were pooled together, and total RNA was extracted using the FastPure Cell/Tissue Total RNA Isolation Kit according to the manufacturer's protocol. cDNA was generated using the HiScript® III All-in-one RT SuperMix Perfect for qPCR kit with 300 ng total RNA. Real-time quantitative PCR was performed using the Taq Pro Universal SYBR qPCR Master Mix in the QuantStudioTM Real-Time PCR System. The PCR cycling conditions were as below: 95°C for 2 min, followed by 40 two-step cycles at 95°C for 15 s and 60°C for 30 s. A list of primers used in this study is presented in Table S2.

Bulk RNA-seq and data processing

For bulk RNA sequencing, day 30 organoids were collected. Total RNA was extracted using the FastPure Cell/Tissue Total RNA Isolation Kit according to the manufacturer's protocol. A Nanodrop 2000 spectrophotometer was used to determine RNA concentration and purity. Agilent 2100 Bioanalyzer and 2100 RNA nano 6000 assay kit were used to evaluate the integrity of RNA samples. Briefly, for samples C3, C4, C6, and C9 (hmSpVO_rep1), the libraries were constructed using TruSeq Stranded mRNA LT Sample Prep Kit and were sequenced on the Illumina HiSeq X Ten platform. For samples of hmSpVO_rep2 and hmSpVO_ventr, the mRNA was prepared by the TIANSeq mRNA Capture Kit, and the libraries were constructed by the TIANSeq Fast RNA Library Kit. The libraries were sequenced on Illumina NovaSeq 6000.

Clean reads were aligned to the reference genome (GRCh38) using STAR v2.7.10a,[44] and RSEM v1.3.1[45] was used to count the reads mapped to each gene and transcripts per kilobase of exon model per million mapped reads (TPM) was calculated. We achieved this through the nf-core/rnaseq pipeline v3.13.2.[46] Raw data of hESC and hCO was processed the same way. Transcriptomic similarity analysis was performed using single sample GSEA method[47] using GSVA (v 1.44.5) R package, and the enrichment score was min-max scaled for visualization. The normalized difference in dorsal and ventral enrichment scores was regarded as the dorsal signature scores. The list of tissue-specific genes was obtained from the GTEx database.[48] Brain region-specific gene

signatures were obtained from the top 20 genes calculated by voxhunt package (v 1.0.1)[24] and the medulla region-specific genes were obtained from a review of molecular signatures of the medulla oblongata.[19] All the gene lists are provided in Table S3.

scRNA-seq and data processing

For single-cell RNA sequencing, day 30 and day 62 hmSpVOs were collected and dissociated into single cells. Briefly, 6-8 hmSpVOs of the same stage were pooled together. Media was removed after centrifugation at 500 g for 5 min, and then 1 ml dispase was added; organoids were lightly cut with a scissor and digested in the metal bath at 37°C for 30 min. The suspension was centrifuged at 500 g for 5 min to remove the supernatant, and 1 ml trypsin was added to continue digestion at 37°C for 15-30 min. When completely digested, cells were passed through a 40 μm sieve and washed with DPBS+10% BSA 2-3 times for further experiments. For quality control, the cell viability should be above 80%. Cells were loaded onto the 10X Chromium Single Cell Platform (10X Genomics) at a concentration of 1,000 cells per μl (Single Cell 3′ library V3) as described in the manufacturer's protocol. GEMs (Gel Bead in Emulsion) were constructed for single-cell separation according to the number of cells to be harvested. After GEMs were formed, GEMs were collected for reverse transcription in a PCR machine for labeling. Then, the GEMs were oil-treated, and the amplified cDNA was purified by magnetic beads and then subjected to cDNA amplification and quality inspection. The 3' Gene Expression Library was constructed with the quality-qualified cDNA. After fragmentation, adaptor ligation, sample index PCR, etc., the library was quantitatively examined and sequenced on the Illumina Novaseq 6000 instrument using 150-base-pair paired-end reads.

To obtain count matrices, reads were aligned to the human genome GRCh38 (v 3.0.0, provided by 10X genomics) using Cell Ranger (v 6.1.2) with the default parameters. Downstream analysis was performed using the R package Seurat (v 4.3.0).[39] For quality control, cells with detected genes between 500 to 5000, UMI count between 4000 to 20000, and the fraction of mitochondrial genes <10% were kept as high-quality cells. Doublets were detected using DoubletFinder (v 2.0.3)[40] and removed. Counts were normalized by the total expression of that cell, multiplied by a scale factor of 10,000, and log-transformed, and then the top 2000 highly variable genes were detected (NormalizeDataand FindVariableFeatures function in Seurat).

For data integration and annotation, the batch effect was removed by MNN method[49] in the SeuratWrappers package (v 0.3.1). After scaling gene expression and performing dimensional reduction, we visualized cells using Uniform Manifold Approximation and Projection (UMAP) embedding. The top 20 dimensions were used to identify neighbors of cells and clusters with a resolution of 1. Cluster annotations were labeled with canonical markers. We first classified neuronal and non-neuronal clusters with the expression of neuronal markers (STMN and DCX) and early neurogenesis markers (SOX2 and NES) as previously defined.[8,12] Then, non-neuronal clusters were divided into the neural progenitor cell (NPC) cluster (expressing SOX2) and the intermediate progenitor (IP) cluster (expressing NHLH1 and INA[50]). The neuronal clusters were divided into the excitatory neuron cluster (ExN, expressing SLC17A6), the inhibitory neuron cluster (InN, expressing GAD1, GAD2, and SLC32A1), and the immature neuron cluster (IM, not expressing neuron type-specific markers).

We compared the transcriptome similarity with published developing human brain (5–14 postconceptional weeks (pcw)) scRNA-seq data[23] using anchor-based label transfer implemented in Seurat. To do that, we first subset 100k cells randomly and integrated using each donor as a batch factor with the IntegrateData function for the reference dataset. Then, anchors between the query and reference dataset were identified and filtered using the FindTransferAnchors function with the top 30 dimensions. Then, the prediction score was calculated using the TransferData function. The cell type and region similarity (defined as the mean prediction score of each cell type) were visualized with a heatmap. We further projected our data on the reference UMAP plot using the MapQuery function.

To examine the regional identity of samples, we performed unbiased spatial mapping of mature neuron clusters (ExN and InN) using the voxhunt R package, then brain region similarity was plotted in a sagittal view or by barplot. To compute spatial correlation patterns of the single-cell transcriptome to the medulla dorsal-ventral subregions, we used the AUCell package (v 1.18.1) to calculate the enrichment score for each cell type and then Z-scaled for visualization.

To assess the transcriptomic similarity of hmSpVOs with different medullary nuclei, we used the same method described above to calculate the enrichment scores. Genes with top 20 fold change and $p<0.05$ were selected as gene signatures for each nucleus compared to other nuclei by using the Allen Brain human brain microarray dataset (https://human.brain-map.org) (ages range from 24 to 57 years old) (Table S3). The data from the left and right hemispheres of the same nucleus were merged for analysis. To understand potential subnucleus-specific features, we analyzed relative gene expressions for Vo (MAFB and FN1), Vi (IRX2, KCNG4, PDE1C, and ZBTB16), and Vc (TAC1, BAIAP3, CAMK2A, CALB2, and CALB1) as reported by Marín et al.[26] Gene expressions with min-max scaled log (counts per 10 k+1) were plotted for ExN and InN, respectively.

We performed trajectory analysis using the monocle3 package (v 1.3.1)[51] with default parameters, and the NPC cluster was chosen as the root node to order cells. Ridgeline plot of pseudotime was performed by ggridges (v 0.5.4) package for different cell types. The pseudotime heatmap of interested genes was plotted using the ClusterGVis (v 0.1.0) package. We also performed RNA velocity analysis using scvelo (v0.2.5)[43]with the scv.tl.velocity function in ''stochastic'' mode and the velocity time was calculated to represent the differentiation trajectory.

To directly compare hmSpVOs to other region-specific brain organoids, we integrated single-cell RNA-seq data from hCOs (late stage, day 72 and 79),[8] hThOs (late stage, day89),[12] and hmSpVOs using harmony (v 0.1.1).[42] After normalization, the top 2000 variable features were used to scale data and perform principal component analysis (PCA). Organoids datasets were integrated based on the top 20 PCs using the function RunHarmony() with default parameters, and the top 20 dimensions were used to identify neighbors of cells and clusters with a resolution of 1.8. Neuronal and non-neuronal clusters were defined as described above. Next, we

focused on the neuronal clusters for further analysis. Marker-positive cell fractions were defined as cells with marker gene count > 0 / total neuronal cells. Differential analyses were performed using the FindMarkers() function in Seurat with logfc.threshold = 0 parameter using wilcox test. Genes with $\log_2$ fold change > $\log_2(1.2)$, adjust p value < 0.01, and the absolute value of the difference (pct.1-pct.2) > 0.1 were defined as statistically significant.

Retrograde labeling

For the retrograde tracing experiment, 300 nl of pAAV-hSyn-EGFP-3XFLAG-WPRE retrograde tracer virus (1.69×10^{13} vg/ml) was injected into either the hThO or hmSpVO region of hSTOs by microinjection using the RWD R480 glass microelectrode injection pump and glass microelectrodes prepared by the RWD MP-500 micropipette puller. Microinjected hSTOs were cultured as usual, and three weeks later, GFP fluorescence could be observed in the corresponding non-injected region. At this point, hSTOs were collected and processed for immunostaining, and the number of $MAP2^+$, $GFAP^+$, $vGLUT2^+$, and $PAX2^+$ cells among the GFP^+ population was quantified. For hThO-to-hmSpVO tracing, virus was injected into the hThO region and quantification was done for the hmSpVO region; for hmSpVO-to-hThO tracing, virus was injected into the hmSpVO region and quantification was done for the hThO region.

Anterograde tracing

For the anterograde tracing, 300 nl of rAAV2/1-hSyn-Cre-WPRE-hGH polyA virus (1.09×10^{13} vg/ml) was injected into the hmSpVO region, and 300 nl of rAAV2/9-EF1a-DIO-EGFP-WPRE- hGH polyA virus (5.20×10^{12} vg/ml) was injected into the hThO region of hSTOs by microinjection using the RWD R480 glass microelectrode injection pump and glass microelectrodes prepared by the RWD MP-500 micropipette puller. Microinjected hSTOs were cultured as usual, and three weeks later, GFP fluorescence could be observed in the hThO region. At this point, hSTOs were collected and processed for immunostaining, and the number of $TCF7L2^+$ cells among the GFP^+ population was quantified.

Optogenetic stimulation and calcium imaging

For the optogenetic stimulation experiment, 300 nl of rAAV2/1-hSyn-ChrimsonR-tdTomato-WPRE-hGH polyA virus (5.21×10^{12} vg/ml) was injected into the hmSpVO region of hSTOs. Three weeks later, hmSpVO projecting axons expressing tdTomato fluorescence could be observed in the hThO region. Before calcium imaging, hSTOs were cultured in BrainPhys Medium (BrainPhys Neuronal Medium, 0.5% (v/v) N2 supplement, 1% (v/v) B27 supplement, 20 ng/ml BDNF, 100μM Bucladesine sodium and 200 μM ascorbic acid) for at least two weeks. hSTOs were incubated in BrainPhys Medium with Cal-520 (5 μM) and powerload (1:100) on 15-mm coverslip glass in a 35-mm glass-bottom plate placed on a shaker at 37°C with 5% CO_2 for 30 minutes, then the media was replaced with fresh BrainPhys Medium. After another 30 min incubation at 37°C with 5% CO_2, calcium changes were recorded with a 20X objective, ChrimsonR-tdTomato$^+$ hmSpVO projecting axons in hThOs were stimulated with 561-nm light under a Nikon CSU-W1 Sora confocal microscope. The stimulation was performed in the thalamic region (hThOs) away from the viral injection site in hmSpVOs. Fluorescent signals for hSyn-ChrimsonR-tdTomato and Cal-520 were captured before stimulation to ensure no ChrimsonR-tdTomato$^+$ thalamic cell bodies were in the stimulation area. Spontaneous activity was recorded for 1 min, followed by stimulation for 100 msec and recording for 10 sec (10 cycles), and ended by a 30-sec recording of spontaneous activity. Tracings of single-cell calcium surges and deltaF/F values were analyzed using Fiji/ImageJ to get raw fluorescent intensity over time for an ROI. GraphPad Prism was used to apply the Savitzky-Golay filter. As controls, CNQX (20 μM) and AP5 (50 μM) were added before calcium imaging.

MEA assay

The microelectrodes arrays of the six-well plate were used to detect electrophysiological activity. Before detection, hmSpVOs sections were cultured at the air-liquid interface in BrainPhys Medium for more than two weeks. On the day of recording, hmSpVOs sections were scraped off the transwell membrane, transferred onto the MEA plate, and the medium was removed. Then, one drop (5 μl) of Matrigel was added to cover the section. After 5 min incubation at 37°C with 5% CO_2, 200 μl BrainPhys Medium was added to cover the section, and the plate was returned to the incubator for 1-2 hours. Electrophysiological recording can then be performed. The recording was performed using the Maestro pro MEA system (Axion Biosystems), and the data was analyzed with the AxIS Navigator (Axion Software) according to the manufacturer's spontaneous neural configuration. Neural Metric Tool (Axion Software) was used to plot electrode array activity. The spike-detecting threshold was set to six standard deviations with an adaptive threshold crossing method, and the spike bursts were identified using an ISI threshold requiring a minimum number of five spikes with a maximum ISI of 100 ms. For chemical treatment, activities were recorded before and after adding either Muscimol (50 μM), R-baclofen (25 μM), CNQX (20 μM) and AP5 (50 μM), Bicuculline (50 μM) or CGRP (1 μM) to the culture.

Electrical stimulation and recording

hSTOs were plated onto the 4096-channel high-density 3D microelectrode array (HD-MEA) flattened with a translucent polyester membrane filter. The hSTOs were settled down for 20 min. Then, the recording was performed using the BioCam Duplex MEA platform with HD-MEA Accura chips (3Brain GmbH, Lanquart, Switzerland). Electrodes in the hmSpVO region (red) were selected for electrical stimulation. Each electrode had a 21 μm × 21 μm area size. 2 adjacent electrodes were used as the positive and 2 as the negative pole for the stimulation. Positive and negative poles were separated by one electrode in the HD-MEA. Stimulation duration was 50 μs, and intensity was 65 μA. Stimulations were introduced 10 times, separated by 10 sec. BrainWave 5 software was used

to analyze data. Raw data were passed through a high-pass filter of 100 Hz, followed by spike detection and sorting. The discharge electrode data in the non-fluorescent region (i.e., the hThO region) were selected and analyzed.

QUANTIFICATION AND STATISTICAL ANALYSIS

Data were presented as mean ±SD or SEM. The paired or unpaired two-tail student's T-test and multiple comparison analysis testing with ANOVA were used to determine the statistical significance (GraphPad Prism 8.2.0). Statistical tests and biological replicates for each experiment were indicated in the figure legends and Table S1. Statistical significance is presented with asterisks: *$p<0.05$, **$p<0.01$, ***$p<0.001$, ****$p<0.0001$.

Cell number quantification

Cell numbers in cryosections were obtained using Analyze Particles in ImageJ (Fiji). Four random regions were calculated for area and cell number for each slice. Then, the total cell number was divided by the total area to obtain the number of cells/area (mm^2). One to two random slices were selected for each organoid for quantification.

Edge axon bundle width quantification

In hmSpVOs, the edge axon bundle was defined as a pathway near the organoid edge enriched with NF^+ axons devoid of $MAP2^+$ dendrites. Because the axon bundles in hThOs were not organized as uniformly as in hmSpVOs (i.e., edge NF^+ axon bundles were not uniformly separated from $MAP2^+$ regions as in hmSpVOs), the edge axon bundle in hThOs was defined as the peripheral tract enriched with NF^+ axons regardless of the presence or absence of $MAP2^+$ dendrites. The width of the edge axon bundles of each organoid was measured in whole-mount staining of organoids. Specifically, it was calculated by averaging the axon bundle width measured at four locations (0°/top, 90°/right, 180°/down, and 270°/left) around the organoid periphery.

Projection quantification

Axon projections were quantified using ImageJ (Fiji). ROIs were manually drawn to cover the regions of projecting and targeted organoids, respectively, and the areas of projecting and targeted organoids were quantified. Using Threshold, adjustment was performed to include the fluorescence signal-positive area in the targeted organoids. The percentage of the signal-positive area per targeted ROI area (PSAT) was calculated using the Analytic-measure. The normalized percentage of fluorescence coverage (%/mm^2) was then calculated by dividing PSAT by the area of the projecting organoid. The maximum axonal bundle width was measured using ImageJ (Fiji) by manually measuring the widest area of the axon bundle in the slice. One to two random slices were selected for each organoid for quantification.